JGR Atmospheres

RESEARCH ARTICLE
10.1029/2022JD037679

Climatology of Clear-Air Turbulence in Upper Troposphere and Lower Stratosphere in the Northern Hemisphere Using ERA5 Reanalysis Data

Ju Heon Lee[1], Jung-Hoon Kim[1], Robert D. Sharman[2], Joowan Kim[3], and Seok-Woo Son[1]

[1]School of Earth and Environmental Sciences, Seoul National University, Seoul, South Korea, [2]National Center for Atmospheric Research, Boulder, CO, USA, [3]Department of Atmospheric Science, Gongju National University, Gongju, South Korea

Key Points:

- Spatial and temporal distributions of Clear-Air Turbulence (CAT) indices for 41 years in the Northern Hemisphere are derived using the highest resolution of reanalysis data
- The CAT potentials are high in three regions: the East Asian, Eastern Pacific, and Northwestern Atlantic regions due to upper-level jets
- Increasing trend of CAT potentials is the largest in East Asia due to warming in tropics and cooling over the Eurasian continent, which have a high impact on transpacific flights

Correspondence to:
J.-H. Kim,
jhkim99@snu.ac.kr

Citation:
Lee, J. H., Kim, J.-H., Sharman, R. D., Kim, J., & Son, S.-W. (2023). Climatology of Clear-Air Turbulence in upper troposphere and lower stratosphere in the Northern Hemisphere using ERA5 reanalysis data. *Journal of Geophysical Research: Atmospheres*, *128*, e2022JD037679. https://doi.org/10.1029/2022JD037679

Received 17 AUG 2022
Accepted 19 DEC 2022

Author Contributions:
Conceptualization: Jung-Hoon Kim
Data curation: Ju Heon Lee
Formal analysis: Ju Heon Lee, Jung-Hoon Kim, Robert D. Sharman, Joowan Kim, Seok-Woo Son
Funding acquisition: Jung-Hoon Kim
Investigation: Ju Heon Lee, Jung-Hoon Kim, Robert D. Sharman, Joowan Kim, Seok-Woo Son
Methodology: Jung-Hoon Kim, Robert D. Sharman
Project Administration: Jung-Hoon Kim
Resources: Jung-Hoon Kim
Software: Ju Heon Lee

Abstract Spatial and temporal distributions of Clear-Air Turbulence (CAT) in the Northern Hemisphere were investigated using 41 years (1979–2019) of the European Centre for Medium-range Weather Forecast Reanalysis version 5 (ERA5) data. We used two groups of CAT diagnostics to determine occurrence frequencies: (a) commonly used empirical turbulence indices (TI1, TI2, and TI3) and their components [vertical wind shear (VWS), deformation, -divergence, and divergence tendency], and (b) theoretical instability indicators [Richardson number (Ri), potential vorticity (PV), and Brunt-Väisälä frequency]. The empirical indices showed high frequencies of moderate-or-greater (MOG)-level CAT potential over the East Asian, Eastern Pacific, and Northwestern Atlantic regions in winter. Over East Asia, the entrance region of strong upper-level jets showed the highest frequencies in TI1, TI2, and TI3 due mainly to strong VWS. The Eastern Pacific and Northwestern Atlantic areas near the exit region of jets had relatively high frequencies of these indices and also Ri. PV frequency was high on the southern side of jet primarily due to negative relative vorticity. Long-term increasing trends of MOG-level CAT potential also appeared in those three regions mainly due to warming in lower latitudes. The most significant increasing trend was found over East Asia, due to the strengthening of the East Asian jet and increased VWS due to the strong meridional temperature gradients in the mid-troposphere induced by warming in the tropics and cooling in eastern Eurasia. These trends over East Asia, if continued, are expected to be of importance to efficient aviation operations across the northwestern Pacific Ocean.

Plain Language Summary Strong bumpiness of cruising aircraft can lead to physical injuries for crews and passengers, which is mostly occurred due to atmospheric turbulence by enhanced wind shear near upper-level jet stream. Spatial characteristics of turbulence and their long-term trends at cruising altitude in Northern Hemisphere were examined using the up-to-date global reanalysis data. The result showed that East Asia, Eastern Pacific, and Northwestern Atlantic regions have a higher frequency of turbulence than other areas. In particular, East Asia was found to be the highest frequency and the largest increasing trend of strong turbulence, which is collocated with a heavy air-traffic region between East Asia and North America across the North Pacific Ocean. This implies that the potential of encountering turbulence over East Asia could be increased further, if the jet stream will be strengthened continually due to climate change in this region.

1. Introduction

The jet stream and associated vertical wind shears (VWSs) are strongest in middle latitudes in the upper troposphere (z = 8–12 km), and their existence is largely explained by the meridional temperature gradient (MTG) between the tropics and polar regions via the thermal wind relation (e.g., Holton, 1992; Lee et al., 2019). Jets are closely associated with dynamic weather phenomena such as storm tracks and cyclogenesis. However, they are also responsible for aviation weather hazards including upper-level turbulence encountered by cruising aircraft in the upper troposphere and lower stratosphere (UTLS) (e.g., Kim et al., 2016; Kim & Chun, 2011; Sharman et al., 2012). These turbulence encounters are commonly referred to as Clear-Air Turbulence (CAT) which often occurs in the vicinity of the jet stream without visually detectable convective clouds (e.g., Kim et al., 2011, 2018; Lester, 1994; Sharman et al., 2006). The CAT may be generated by a variety of mechanisms, including but not limited to, shear instability, frontogenesis near upper-level jet/frontal systems (Dutton & Panofsky, 1970; Ellrod & Knapp, 1992), and emissions of inertia gravity waves via geostrophic adjustments at the exit region

Supervision: Jung-Hoon Kim, Robert D. Sharman, Seok-Woo Son
Validation: Ju Heon Lee, Jung-Hoon Kim, Robert D. Sharman, Joowan Kim, Seok-Woo Son
Visualization: Ju Heon Lee
Writing – original draft: Ju Heon Lee
Writing – review & editing: Jung-Hoon Kim, Robert D. Sharman, Joowan Kim, Seok-Woo Son

of jet streams (e.g., Ellrod & Knox, 2010; Koch et al., 2005; Lane et al., 2004; F. Zhang, 2004). Inertial instability developed in anticyclonic shear and curvature flows may also be an important source for CAT (e.g., Kim et al., 2014; Knox, 1997).

Moderate-or-greater (MOG) intensity CAT can cause structural damage to aircraft and serious physical injuries to crews or passengers. These problems in turn lead to economic loss and flight delays (Kim et al., 2016, 2018; Sharman & Pearson, 2017; Sharman et al., 2006; Wolff & Sharman, 2008). Therefore, long-haul flight routes across the oceans and continents need to be planned to minimize possible CAT encounters for efficient and safe flights. However, CAT forecasting is challenging due to its isolated nature and small-scale motion (turbulent eddies of ∼10–1,000 m horizontal scale) compared to current numerical weather prediction (NWP) model resolutions (e.g., Lester, 1994; Sharman et al., 2014; Sharman & Pearson, 2017; Sharman et al., 2006). However, CAT can be diagnosed with some reliability from NWP models using empirical turbulence indices and theoretical instability indicators under the assumption that the turbulence originates at resolved scales and cascades down to smaller eddies that may affect aircraft (e.g., Cho & Lindborg, 2001; Kim & Chun, 2010; Kim et al., 2011, 2018; Sharman et al., 2014, 2006).

As the MTGs have increased in some regions mainly due to global warming, jet streams have correspondingly modulated over the past decades (e.g., Lee et al., 2019; Lv et al., 2021). Consequently, CAT potential is expected to increase over some regions. Jaeger and Sprenger (2007) showed spatial distributions and trends of four CAT diagnostics in the UTLS in the Northern Hemisphere (NH) using the European Centre for Medium range Weather Forecast (ECMWF) Re-Analysis 40 (ERA40) data with T159 (∼90 km) horizontal resolution for 44 years (1958–2001). They identified a 40%–90% frequency increase of CAT according to the diagnostics they used over the North Atlantic, United States, and European sectors. Kim et al. (2016) also showed variations in CAT potential along flight routes during two distinct North Atlantic Oscillation patterns. Lee et al. (2019) analyzed temperature and VWS trends in the North Atlantic region from 1979 to 2017 using three reanalysis datasets from the ECMWF, National Centers for Environmental Prediction/National Center for Atmospheric Research, and Japanese Meteorological Agency. They found an intensification of VWS and therefore CAT potential of about 11%–17% for the study period. Similar trends are found on several future projections of climate model data, showing that the occurrence frequency of CAT will be stronger along with the modified jet stream (Storer et al., 2017; Williams, 2017; Williams & Joshi, 2013). Therefore, it becomes important to understand the details of CAT climatology in the NH during future climate change.

This study aims to analyze historical patterns and trends of CAT in the recent four decades (1979–2019) using the highest resolution reanalysis data available and extends the findings of previous studies in three ways. First, we calculate a total of 10 empirical and theoretical diagnostics to identify various generation mechanisms of CAT near upper-level jets and their contributions to CAT climatology, whereas previous NH CAT climatology studies used relatively fewer diagnostics. Second, we examine the long-term trends of CAT diagnostics over the entire NH by expanding the previous studies which investigated the trends of CAT potential only in specific areas. Finally, we focus on CAT potential over the East Asian region where the increasing trend of CAT in NH is the strongest in response to climate change. In Section 2, the data and methodology used in this study are introduced. The results of CAT climatologies and interpretations are discussed in Section 3, followed by a summary and conclusions in Section 4.

2. Data and Methodology

In this study, we used the ECMWF Re-Analysis version 5 (ERA5) data (Hersbach et al., 2020), which has $0.25° \times 0.25°$ horizontal grid spacing over the global domain. At the moment, the ERA5 has the finest resolution among existing global reanalysis datasets. The higher horizontal resolution facilitates a more reliable identification of CAT features in local areas. To examine CAT potential, we used 6-hourly data (00, 06, 12, and 18 UTC) from the 41-year record of ERA5 from January 1979 to December 2019. We calculated the CAT potential in the UTLS using 12 vertical layers between 100 and 500 hPa levels (100, 125, 175, 150, 200, 225, 250, 300, 350, 400, 450, and 500 hPa), which has sufficient vertical resolution to calculate variabilities associated with vertical shear and upper-level jet streams near the tropopause and typical cruising levels (e.g., 250 hPa) (Kim et al., 2020).

We used two groups (which we define as empirical indices and theoretical instability indicators) of CAT diagnostics. The empirical diagnostics used are the Turbulence Index versions 1, 2, and 3 (TI1, TI2, and TI3) and their

components [VWS, deformation (DEF), -divergence (DIV), and divergence tendency (DVT)]. The TI1 index has been widely used as one of top diagnostics for CAT forecasting at several weather prediction centers (e.g., Kim et al., 2018). It is a product of VWS and DEF representing CAT caused by shear instability and frontogenesis (Ellrod & Knapp, 1992). Shear instability diagnosed by VWS is strong above and below the jet stream (Kim & Chun, 2010). Frontogenesis caused by DEF appears on the cyclonic shear side of the jet stream due to strong MTGs, which increases VWS in accordance with thermal wind relationship (Ellrod & Knapp, 1992). The TI2 additionally considers convergent flow (-DIV) related to the development of upper-level frontal zones, which in turn strengthens VWS (Ellrod, 1985). Finally, TI3 replaces the divergence term in TI2 with divergence tendency (DVT) which may capture the generation of inertia gravity waves via geostrophic adjustment processes or spontaneous imbalance (e.g., Ellrod & Knox, 2010; Knox et al., 2008). The TI1, TI2, and TI3 are calculated by the following equations.

$$\mathrm{TI1} = \mathrm{VWS} \times \mathrm{DEF} = \left(\left(\frac{\partial u}{\partial z}\right)^2 + \left(\frac{\partial v}{\partial z}\right)^2\right)^{1/2} \left(\left(\frac{\partial u}{\partial x} - \frac{\partial v}{\partial y}\right)^2 + \left(\frac{\partial v}{\partial x} + \frac{\partial u}{\partial y}\right)^2\right)^{1/2} \tag{1}$$

$$\mathrm{TI2} = \mathrm{VWS} \times (\mathrm{DEF} - \mathrm{DIV}) = \left(\left(\frac{\partial u}{\partial z}\right)^2 + \left(\frac{\partial v}{\partial z}\right)^2\right)^{1/2} \left[\left(\left(\frac{\partial u}{\partial x} - \frac{\partial v}{\partial y}\right)^2 + \left(\frac{\partial v}{\partial x} + \frac{\partial u}{\partial y}\right)^2\right)^{1/2} - \left(\frac{\partial u}{\partial x} + \frac{\partial v}{\partial y}\right)\right] \tag{2}$$

$$\mathrm{TI3} = \mathrm{TI1} + \mathrm{DVT}, \quad \mathrm{DVT} = C\left|\left(\frac{\partial u}{\partial x} + \frac{\partial v}{\partial y}\right)_{t2} - \left(\frac{\partial u}{\partial x} + \frac{\partial v}{\partial y}\right)_{t1}\right| \tag{3}$$

where u is zonal wind speed and v is meridional wind speed. The DVT was calculated by using the difference between the present data (t2) and the previous data 6 hours earlier (t1). The empirical constant value C is a scaling parameter to adjust the magnitude of DVT to be of the same magnitude as TI1, which was estimated by probability density functions (PDFs) following the method outlined in previous studies (Lee et al., 2020). From the PDFs it was found that the peaks appeared around 1.82×10^{-7} s^{-1} and 2.37×10^{-5} s^{-1} for TI1 and DVT, respectively. Therefore, we set the scaling parameter of C to be 0.01, making DVT have a similar magnitude to TI1 (e.g., Lee et al., 2020).

In addition to the empirical diagnostics TI1, TI2, and TI3 defined above, we also considered three "theoretical" instability diagnostics: the Brunt-Väisälä frequency (N^2), Richardson number (Ri), and potential vorticity (PV), which are directly related to convective, Kelvin-Helmholtz, and inertial instabilities, respectively. These diagnostics are termed "theoretical" here since they are based on various simplified instability theories. Convective instability is generated when N^2 becomes negative. Statically unstable flows are associated with convective overturning, which can lead to CAT (e.g., Jaeger & Sprenger, 2007). The Ri less than some small number indicates Kelvin-Helmholtz instability when VWS is large and/or N^2 is small. We set the threshold of Ri to $0 < \mathrm{Ri} < 1$ in this study to separate Kelvin-Helmholtz instability from convective instability when $N^2 < 0$ (e.g., Abarbanel et al., 1984; Jaeger & Sprenger, 2007; Kim & Chun, 2010, 2012). The condition $\mathrm{PV} < 0$ is used here primarily to identify regions of inertial instability (e.g., Kim et al., 2014; Knox & Harvey, 2005; Sato & Dunkerton, 2002; Trier & Sharman, 2016) which may be favorable for the generation of CAT. Inertial instability is primarily generated by negative relative vorticity in strong anticyclonic shear and curvature flows in the NH (e.g., Holton, 1992; Jaeger & Sprenger, 2007; Thompson et al., 2018). However, as with the Ri, PV can be negative when the absolute vorticity is positive and $N^2 < 0$ as well. The theoretical indicator equations are as follows.

$$N^2 = \frac{g}{\theta}\frac{\partial \theta}{\partial z} \tag{4}$$

$$\mathrm{Ri} = \frac{N^2}{\mathrm{VWS}^2} \tag{5}$$

$$\mathrm{PV} = \frac{1}{\rho}(\zeta + f)\frac{\partial \theta}{\partial z} \tag{6}$$

where θ, ζ, ρ, and f represent the potential temperature, the relative vorticity, the air density, and the Coriolis parameter, respectively.

To examine the spatial and temporal distributions of MOG-level CAT, reliable MOG thresholds must be established for each CAT index. Thresholds of the theoretical instability indices are provided according to dynamical considerations, and we assume here that if these thresholds are satisfied, MOG turbulence occurs somewhere with the given grid cell. MOG thresholds for the empirical indices can be determined by using a log-normal fit to the ERA5 derived PDFs as in Sharman and Pearson (2017) or by calculating a top percentile of the ERA5 derived PDF of each diagnostic as was done in Williams (2017). For consistency with other climatological studies we use the latter approach here. Williams (2017) set the probability of MOG-level CAT to the top 0.4 percentile of the calculated CAT diagnostics. Kim and Chun (2011) and Lee and Chun (2015) found that 3%–4% of CAT incidents occurring over South Korea and East Asia where the strongest jet streams exists were in the MOG category. Wolff and Sharman (2008) and Sharman et al. (2014) estimated climatological upper-level MOG turbulence frequency at 1%–2% based on pilot reports and in situ turbulence observation data from commercial aircraft in United States, respectively. However, the in situ aircraft-based studies only consider turbulence encountered by cruising aircraft and the actual encounter frequency can be underestimated by avoiding already forecasted areas (Colson, 1963; Sharman et al., 2014). Therefore, given that this study focuses on the frequency of CAT in the UTLS near upper-level jet streams, we choose the 95th percentile value as the thresholds of each CAT index for MOG-level CAT (e.g., Lee et al., 2020).

Figure 1 shows the PDFs of the empirical CAT diagnostics (VWS, DEF, DIV, DVT, TI1, TI2, and TI3) for summer (JJA; red histograms) and winter (DJF; blue histograms) during the research period (41 years: 1979–2019). To incorporate two different seasons with one representative threshold for each diagnostic, the 95% values were computed from the sum of summer and winter PDFs for each index, which is indicated by black dashed vertical lines in Figure 1. Here, all PDFs were calculated at a typical cruising altitude of 250 hPa for commercial aircraft in the midlatitude regions (20–60°N) where the climatological jet stream is located. Table 1 shows the determined thresholds of each index.

3. Results

3.1. Case Studies

To assess the veracity of the selected MOG thresholds, we perform four case studies of observed CAT over the North Pacific and North Atlantic regions. The first two cases occurred at 1010 UTC and 1125 UTC on October 11, 2012 involving two flights from Incheon, South Korea to San Francisco and Seattle, respectively. MOG-level CAT was experienced at about 11 km altitude (~225 hPa) when crossing over the Northwestern Pacific Ocean (S.-H. Kim et al., 2022). Here, MOG-level CAT is defined when observed variation of the in situ Quick-Access Recorder data vertical acceleration is more than $\pm 0.7g$ (Lane et al., 2012). Figures 2a and 2b indicate the evolution of the large-scale flow associated with the turbulence events based on the ERA5 derived horizontal wind speed and geopotential height at 225 hPa at 0600 UTC and 1100 UTC. At 0600 UTC, the jet stream (>50 m s^{-1}) including turbulence spots was located over the Northwestern Pacific Ocean. After 5 h at 1100 UTC, the jet was enhanced with the jet core exceeding 70 m s^{-1} on the western side of the turbulence regions. This implies that the difference in wind speed from lower levels had increased around the incident time and consequently the VWS intensified significantly to exceed the determined threshold (1.03×10^{-2} s^{-1}) as shown in Figure 2d and was therefore probably the main source of the turbulence events.

The turbulence driven by this strong VWS was well diagnosed with both the theoretical instability indicators and the empirical indices (Figure 2c). First, Ri < 1 (orange solid contour) was locally located on the eastern side of the turbulence events. Though it did not cover the turbulence spots because of very statically stable conditions in this area ($N^2 > 0$; not shown), the shear instability inducing the MOG-level CAT did occur over the incident region. The empirical indices TI1, TI2, and TI3 also appropriately diagnosed the CAT events by showing high values above the pre-determined thresholds within the incident region. Furthermore, given that their patterns coincided with that of VWS (Figure 2d), we suppose that the empirical indices diagnosed the turbulence events mainly due to the enhanced VWS (Figure 2d). The slightly different patterns of TI1, TI2, and TI3 resulted from high values of the other components (i.e., DEF, -DIV, and DVT; not shown).

Two other cases were examined based on in situ Eddy Dissipation Rate (EDR) reports provided by the Aircraft Meteorological Data Relay (AMDAR) data (NOAA/ESRL, 2011). Here, the level of turbulence intensity is determined by the observed EDR: 0.15–0.22 $m^{2/3}$ s^{-1} for "light," 0.22–0.34 $m^{2/3}$ s^{-1} for "moderate," and >0.34 $m^{2/3}$ s^{-1}

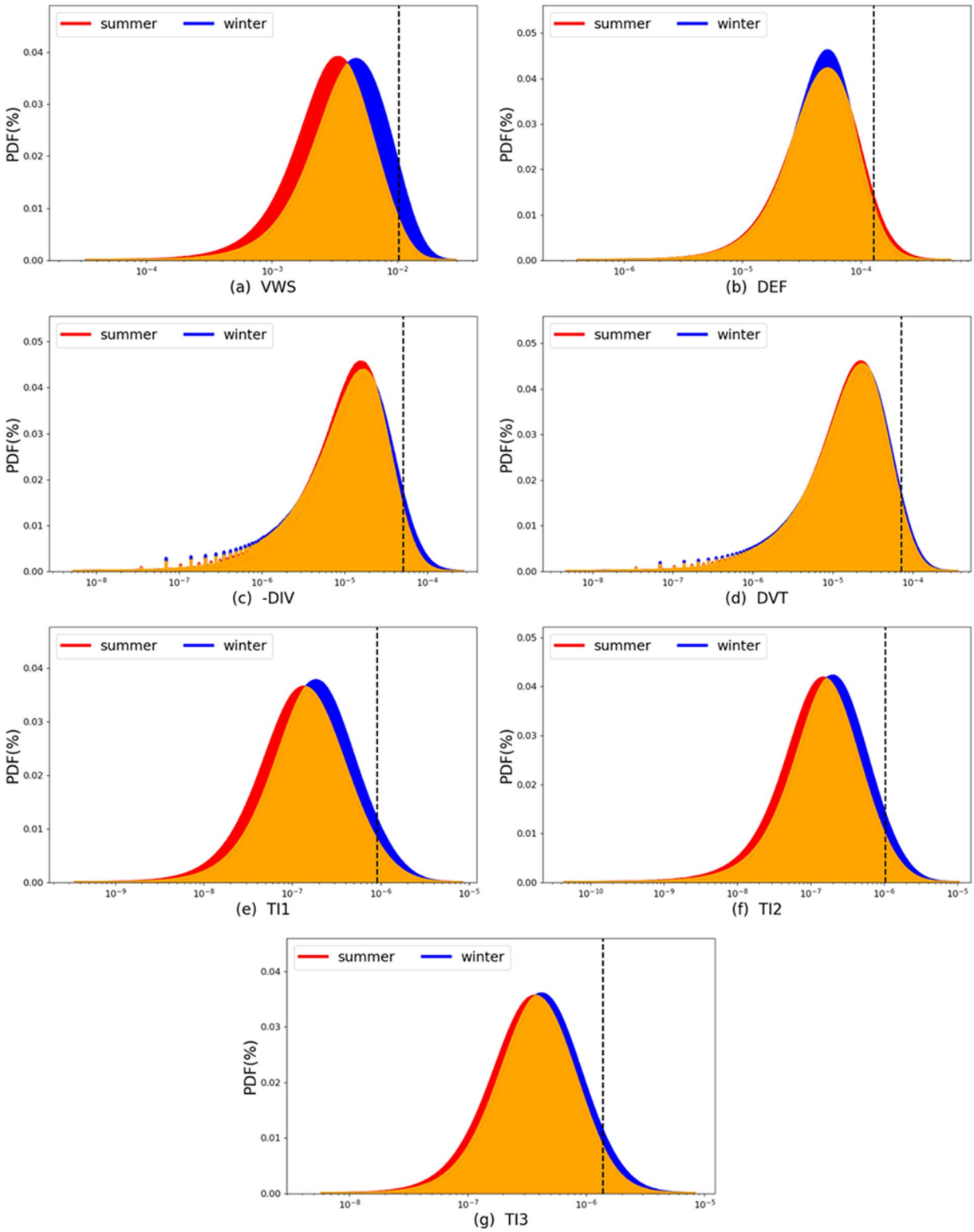

Figure 1. Probability density functions (PDFs) of each Clear-Air Turbulence (CAT) empirical index calculated at 250 hPa in the 20–60°N latitude band for 41 years (1979–2019) of ERA5 data. Red and blue histograms indicate summer and winter seasons, respectively, and orange shows the overlap region between the two seasons. The 95th percentile value is depicted by black dashed vertical line.

Table 1
Moderate-Or-Greater (MOG) Thresholds From the Calculated 95th Percentile Values of the ERA5 Derived Probability Density Functions (PDFs) for the Empirical Clear-Air Turbulence (CAT) Indices at 250 hPa in the 20–60°N for 41 years (1979–2019), and Assumed Thresholds for Theoretical Instability Indicators With Their Units

CAT index	MOG threshold	Unit
VWS	$>1.03 \times 10^{-2}$	s^{-1}
DEF	$>1.29 \times 10^{-4}$	s^{-1}
-DIV	$>5.15 \times 10^{-5}$	s^{-1}
DVT	$>7.18 \times 10^{-5}$	s^{-1}
TI1	$>9.07 \times 10^{-7}$	s^{-1}
TI2	$>1.03 \times 10^{-6}$	s^{-1}
TI3	$>1.39 \times 10^{-6}$	s^{-1}
N^2	<0	s^{-2}
PV	<0	1 PVU
Ri	0 < Ri < 1	Dimensionless

Note. VWS, vertical wind shear; DEF, deformation; -DIV, -divergence; DVT, divergence tendency; N2, Brunt-Väisälä frequency; PV, potential vorticity; Ri, Richardson number.

for "severe" (Sharman et al., 2014). Figures 3a and 3b show the turbulence events occurred at 08 UTC January 26, 2018 over the North Atlantic Ocean and at 07 UTC July 7, 2019 over the North Pacific Ocean, respectively. In the former case (Figure 3a), the determined thresholds detected the widespread region of turbulence on the cyclonic shear side of an anticyclonically curved jet stream at which several light and moderate CAT events were observed. In the latter case (Figure 3b), the determined thresholds correctly captured the local area of MOG-level CAT events at the entrance of jet stream with a strong VWS, which excluded the area of light-level turbulence. This implies that the 95th percentile values of PDFs for TI1–3 properly distinguish the spot of MOG-level CAT. The results of these case studies provide the confidence that the determined thresholds from the previous section are satisfactorily reliable to identify the regions of MOG-level CAT for the purpose of developing a CAT climatology in the NH.

3.2. Horizontal Climatological Distribution

In this section, we provide horizontal distributions of the selected CAT indices to identify spatial patterns of climatologies of upper-level CAT generation mechanisms in the NH. Figures 4–7 show the frequency distributions of each index for the 41 years (1979–2019) at 250 hPa (~34,000 ft or 10.4 km) in the NH for winter (DJF) and summer (JJA) based on the determined thresholds (Table 1). The frequency was calculated as the ratio (%) of the number of values that exceed the thresholds at each grid box in the 6-hourly data during the 41 years, as was done in previous studies (e.g., Jaeger & Sprenger, 2007; Kim & Chun, 2011; Williams, 2017).

Focusing first on winter (Figures 4 and 5), comparing the average zonal wind speed to the frequency of empirical indices above the 95th percentile threshold, the highest frequencies are generally seen on the northern side of the jet. This is consistent with the results of Jaeger and Sprenger (2007) in which the indicators based on DEF such as TI1 were found to be more frequent in cyclonic flows. All three indices, that is, TI1, TI2, and TI3 showed local maxima over East Asian (80–150°E, 30–45°N), Eastern Pacific (170°E–130°W, 35–55°N), and Northwestern Atlantic (80–20°W, 35–60°N) regions near the entrance and exit of the climatological upper-level jets (Figures 4a–4c). Their highest frequencies appeared over East Asia (maximum value of TI1 = 25.84%; TI2 = 27.10%; TI3 = 22.17%) primarily due to VWS (Figure 5a) associated with the East Asian jet entrance region. The acceleration and deceleration of the zonal wind in the upper and lower levels, respectively, driven by opposite Coriolis torques of ageostrophic secondary circulation at the jet entrance strengthens the local VWS in the UTLS.

Secondary local maxima of TI1, TI2, and TI3 were also found over the Eastern Pacific (maximum value of TI1 = 14.57%; TI2 = 12.45%; TI3 = 16.84%) and Northwestern Atlantic (maximum value of TI1 = 11.84%; TI2 = 10.48%; TI3 = 13.52%) located at the exit region of the jet stream. These were induced by large DEF, -DIV, and DVT in the vicinity of the jet exit region as well as large VWS. Large-scale DEF at the exit of the jet and convective flows due to storm tracks in these regions manifested as high frequencies of DEF at the exit region of the Pacific and Atlantic jets (Figure 5b). Large patterns of convergence indicated by -DIV as shown in Figure 5c are due to decreasing wind speed within the exit region of the jet stream. Maximum patterns of DVT at the exit of the jet stream are shown on Figure 5d, which contributes to higher frequencies of TI3 in these regions compared to TI1 and TI2 by additionally considering CAT generation related to inertia gravity waves. Another interesting feature is the locally high frequencies over mountain regions such as Himalaya, Rockies, Alps, and Greenland. These are probably due to mesoscale mountain waves that can be partially resolved by the high resolution ERA5 data and are most apparent in the DEF, DIV, and DVT terms.

On the other hand, the theoretical index Ri correlated with shear instability showed somewhat different patterns from those of empirical indices. Higher frequencies of small Ri occurred over the Eastern Pacific and Northwestern Atlantic regions, while minimum frequencies appeared over East Asia (Figure 4e). The results over the Eastern Pacific and Northwestern Atlantic regions are due to the relatively high frequencies of VWS at the exit region

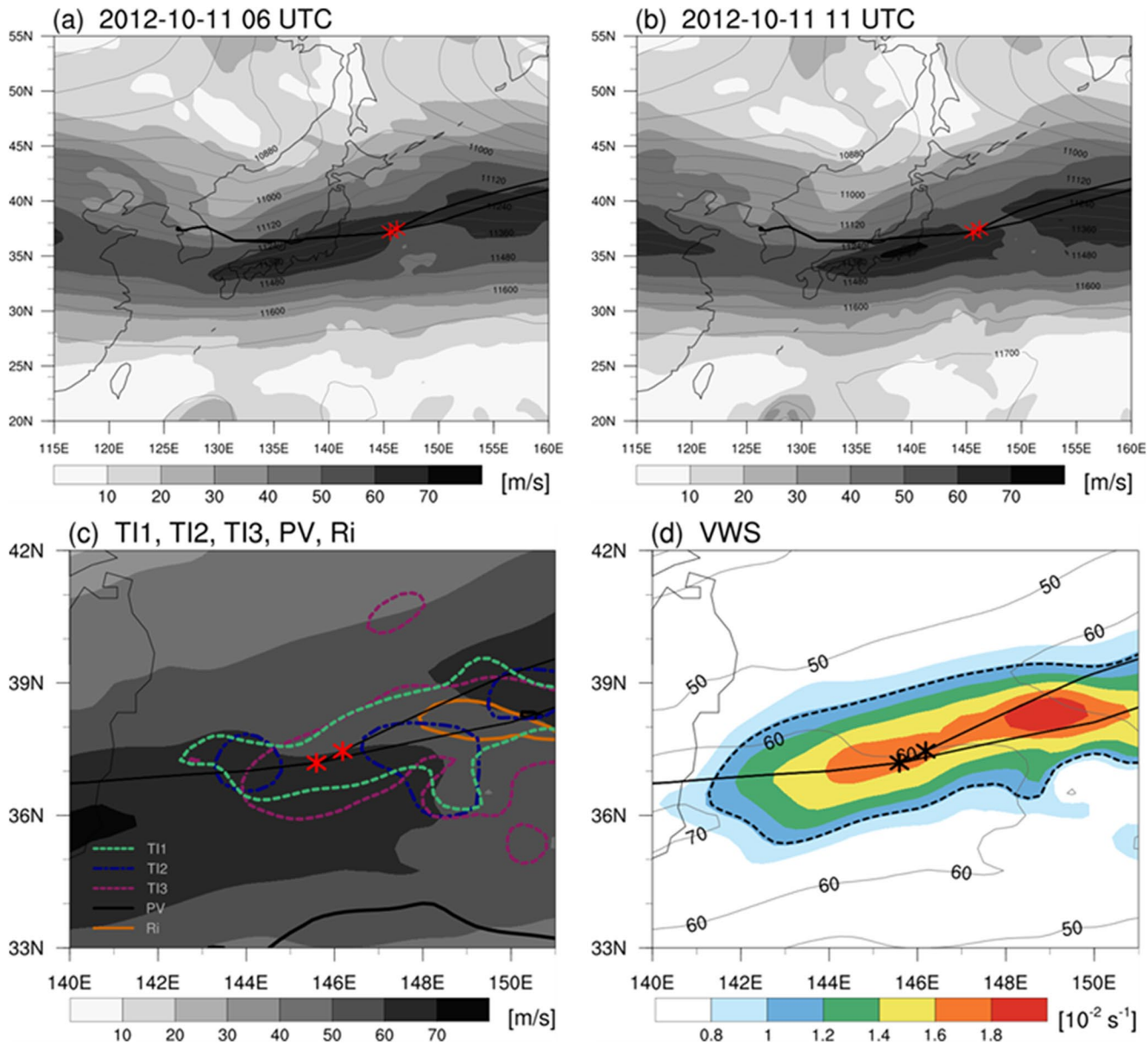

Figure 2. (a and b) Horizontal wind speed (shading) with geopotential height (60 gpm interval; gray contour) on 225 hPa at 0600 UTC and 1100 UTC October 2012, respectively. Clear-Air Turbulence (CAT) indices distributions (c) TI1 = 9.07×10^{-7} s^{-1} (green dashed contour), TI2 = 1.03×10^{-6} s^{-1} (navy dashed-dotted contour), TI3 = 1.39×10^{-6} s^{-1} (purple dotted contour), PV = 0 (black solid bold contour), and Ri = 1 (orange solid contour), (d) vertical wind shear (VWS) (shading) with zonal wind speed at 1100 UTC October 11, 2012 at 225 hPa over eastern Japan. Zonal wind speed is shown by shading and gray contours in (c) and (d) respectively from 10 to 70 m s^{-1} with a 10 m s^{-1} interval. Black dashed contour in (d) represents the moderate-or-greater (MOG) threshold of VWS (1.03×10^{-2} s^{-1}). Flight routes and observed locations of MOG turbulence at 1010 UTC and 1125 UTC October 11, 2012 are depicted by black solid thin lines and red [(a), (b), and (c)] and black [(d)] asterisks.

of the jets (Figure 5a). Moreover, these regions are areas of nominal storm tracks (Figure 4d) involving relatively low static stability that contributes to relatively lowered values of positive Ri. Here, note that magnitude of N^2 frequency is smaller than that of other indices because of insufficient upper-level vertical layers of ERA5 data. Therefore, we focused on a relative frequency distribution indicating CAT potential by N^2 in the NH, instead of an absolute frequency value. In contrast, East Asia had the least frequency of small Ri despite the highest frequency of VWS with maximum value of 35.90% compared with 16.72% in the Eastern Pacific and 11.31% in the Northwestern Atlantic. The results are probably due to highly stable stratospheric air intruding into the mid-troposphere below the jet core by deep tropopause folding over East Asia (e.g., Kim & Chun, 2010), which inhibits small Ri due to the high values of N^2. However, TI1, TI2, and TI3 diagnosed relatively higher CAT potential mainly

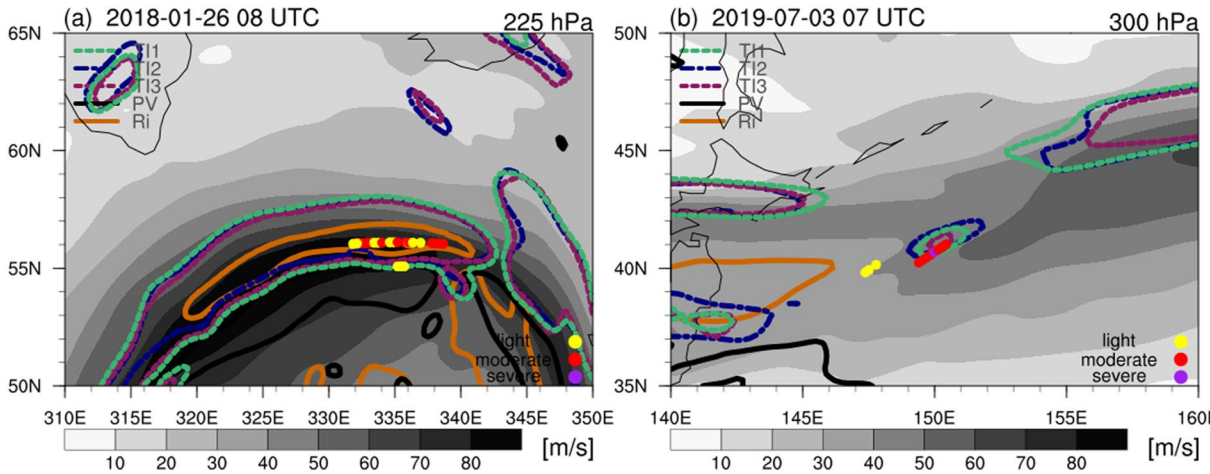

Figure 3. Observed turbulence cases at (a) 0800 UTC January 26, 2018 at 225 hPa over the North Atlantic Ocean and (b) 0700 UTC July 3, 2019 at 300 hPa over the North Pacific Ocean. The locations of the observed turbulence are denoted by yellow, red, and purple dots for light, moderate, and severe level turbulence, respectively. Horizontal wind speed (shading) with Clear-Air Turbulence (CAT) indices distributions are shown: TI1 = 9.07×10^{-7} (green dashed contour), TI2 = 1.03×10^{-6} (navy dashed-dotted contour), TI3 = 1.39×10^{-6} (purple dotted contour), PV = 0 (black solid bold contour), and Ri = 1 (orange solid contour).

by strong VWS even in the highly stratified conditions over East Asia. These results will be further investigated using higher resolution reanalysis data and numerical simulations for CAT cases under strong VWS with highly stratified conditions (e.g., Kim & Chun, 2010; Trier et al., 2022).

The areas of negative PV (Figure 4f) were concentrated mainly on the southern side of the climatological jets where inertial instability is generated by negative values of relative vorticity and relatively low value of Coriolis force in low latitude. The maximum frequency of negative PV was on the anticyclonic shear side of the East Asian jet and is mainly due to the negative values of relative vorticity generated by the strong jet streak over East Asia rather than convective instability (negative N^2 frequency is very rare over East Asia; Figure 4d). Therefore, East Asia is susceptible to CAT caused by inertial/symmetric instability as well. The Eastern Pacific and Northwestern Atlantic regions had low frequencies of PV on the anticyclonic shear side of the climatological jets. Over these regions, the occurrence of CAT by symmetric instability could be from convective instability since frequencies of N^2 are large due to storm tracks (Figure 4d) if absolute vorticity locally becomes positive.

Compared to winter, in summer (Figures 6 and 7), the TI1, TI2, and TI3 frequencies were generally lower and shifted northward due to the northward shift of the weaker jet stream. Local maxima of TI1, TI2, and TI3 still appear over East Asia, the Northwestern Atlantic and additionally over Mediterranean Europe. As shown in Figure 7, the frequencies of the empirical index components also decreased along the weaker summertime jets in the NH. An exception is the frequency of DEF (Figure 7b) which increased and is displaced further north in summer. This change is consistent with the seasonal variation of TI1, TI2, and TI3, indicating that DEF (Figure 7b) has a larger impact than the weakened VWS (Figure 7a) on the occurrence of CAT at 250 hPa in the summer over the East Asian, Northwestern Atlantic, and European regions. In addition, despite the weaker jets, higher frequencies of -DIV and DVT (Figures 7c and 7d) in summer than in winter were found over East Asia, contributing to the maximum frequencies of TI1, TI2, and TI3 there. These may also be related to increased convective activity in this region (Figure 6d) due to the summer monsoon system over East Asia (Yihui & Chan, 2005). In contrast, there was no increase in frequency patterns of -DIV and DVT in the Eastern Pacific and Northwestern Atlantic regions unlike in winter because of the weaker jets and particularly the weakened storm tracks in the UTLS (Hoskins & Hodges, 2019). The summer distribution of CAT coincided well with the distribution of N^2 showing lower frequencies compared to the winter period over these regions. However, there were still relatively high frequencies of -DIV and DVT over North America but lower than in the winter period, which probably derived from mesoscale convective systems developing in this area in the summertime (Prein et al., 2020; Tian et al., 2005). Consequently, in summer as in winter, East Asia still has the highest CAT potential based on the empirical diagnostics.

These results were also identified by the theoretical instability diagnostics. In particular, the Ri distribution in summer (Figure 6e) is distinctly different from that in winter and is similar to the distribution of the empirical

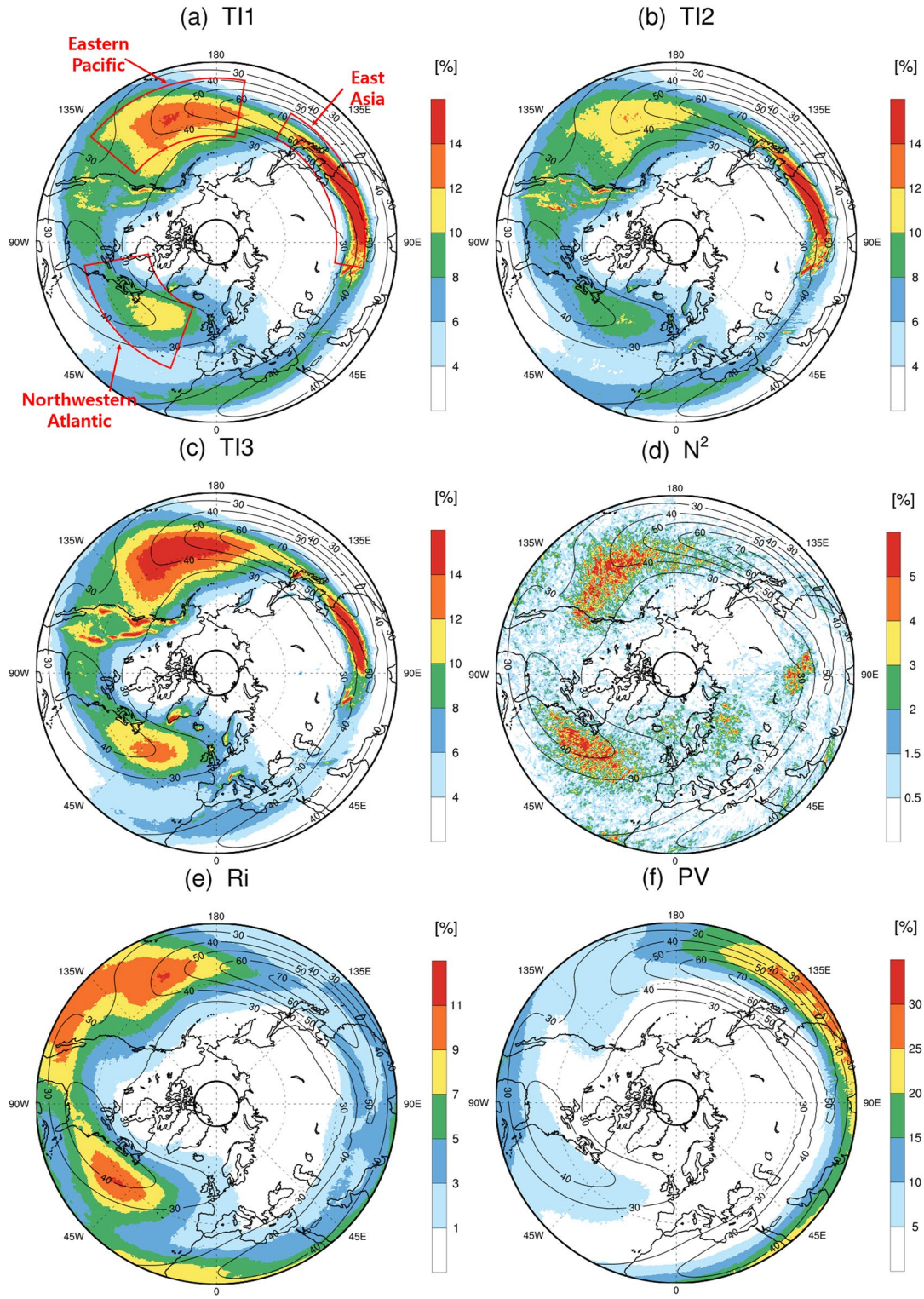

Figure 4. Frequency (%) distributions of Clear-Air Turbulence (CAT) indices (shading) for (a) TI1, (b) TI2, (c) TI3, (d) N^2, (e) Ri, and (f) PV at 250 hPa in the 20–80°N for 41 years (1979–2019) for the winter period (DJF). Averaged zonal wind speeds are also shown as black contours from 30 to 80 m s^{-1} at 10 m s^{-1} intervals.

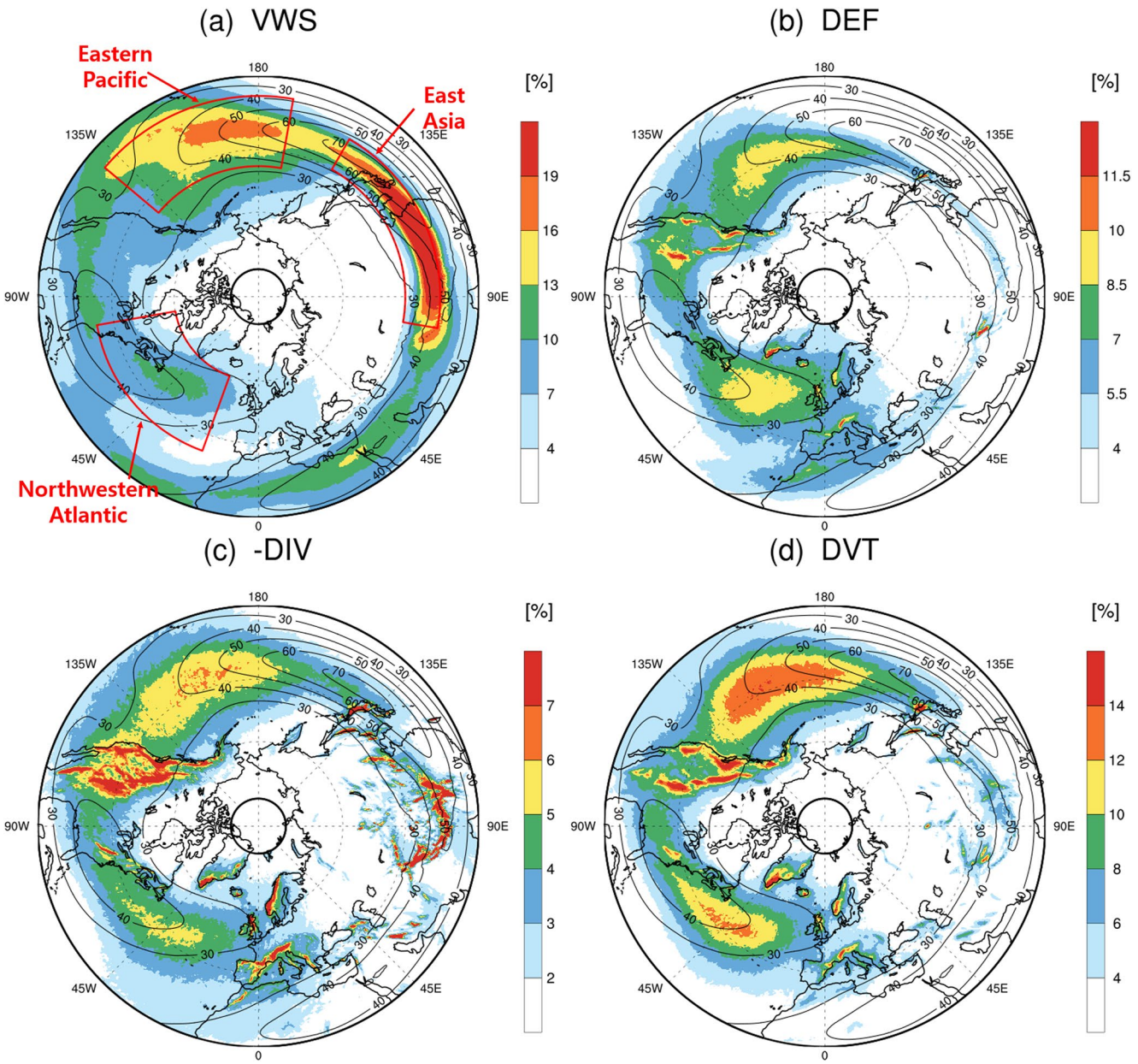

Figure 5. Same as Figure 4, but for (a) vertical wind shear (VWS), (b) deformation (DEF), (d) -divergence (-DIV), and (d) divergence tendency (DVT).

indices with local maxima over East Asia regardless of the weakened VWS (Figure 7a). This is due to convectively low stability associated with the presence of the East Asian monsoon as mentioned above. Similarly, North America has a relative maximum in the frequency pattern of Ri which can be attributed to low stability generated by deep convection rather than weakened shear instability. The higher frequencies of negative PV were on the southern side of the summer jets in the NH but had much lower frequencies than in winter due to the decreased frequencies of negative absolute vorticity associated with the weaker jets.

3.3. Vertical Climatological Distribution

To further demonstrate the relationship between the jet system structures and CAT potential induced by various mechanisms in the UTLS, we display vertical cross-sections of the CAT indices and their components in Figures 8–11. Here, we investigated four zonally averaged regions manifesting significant patterns of CAT potential in the horizontal distributions during the winter and summer periods.

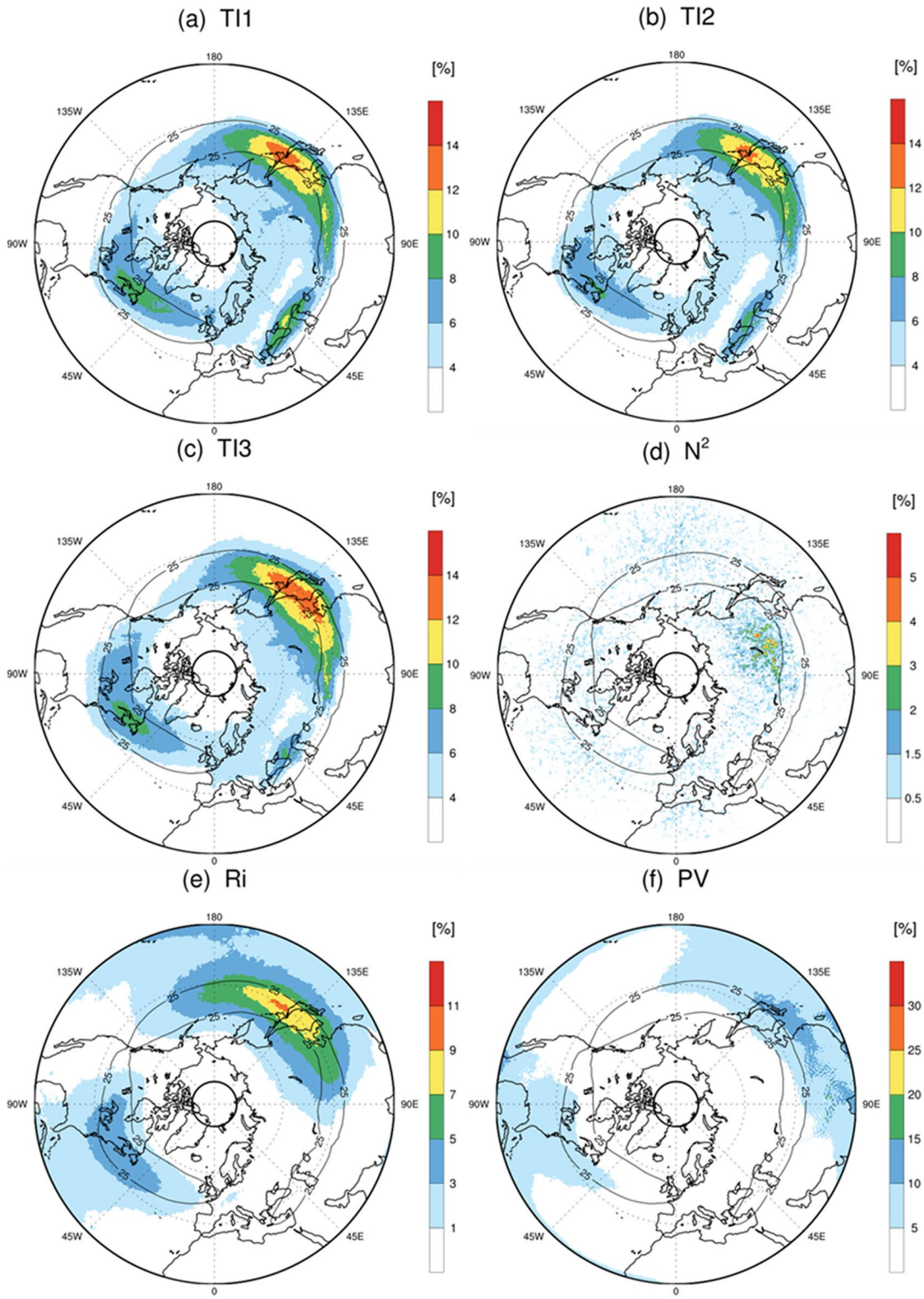

Figure 6. Same as Figure 4, but for the summer period (JJA). Distributions of averaged zonal wind speed are shown as black contours from 25 to 65 m s^{-1} at 10 m s^{-1} intervals.

In Figure 8b over East Asia, the strongest jet cores with zonal wind speed exceeding 50 m s^{-1} are located between 100 and 500 hPa in winter. Accordingly, VWS, -DIV, and DVT became more frequent (Figure 9b) with the maximum frequencies of the empirical indices (i.e., TI1, TI2, and TI3) above and below the jet core. Especially, VWS showed the highest frequencies at all levels among other midlatitude regions due to the strong

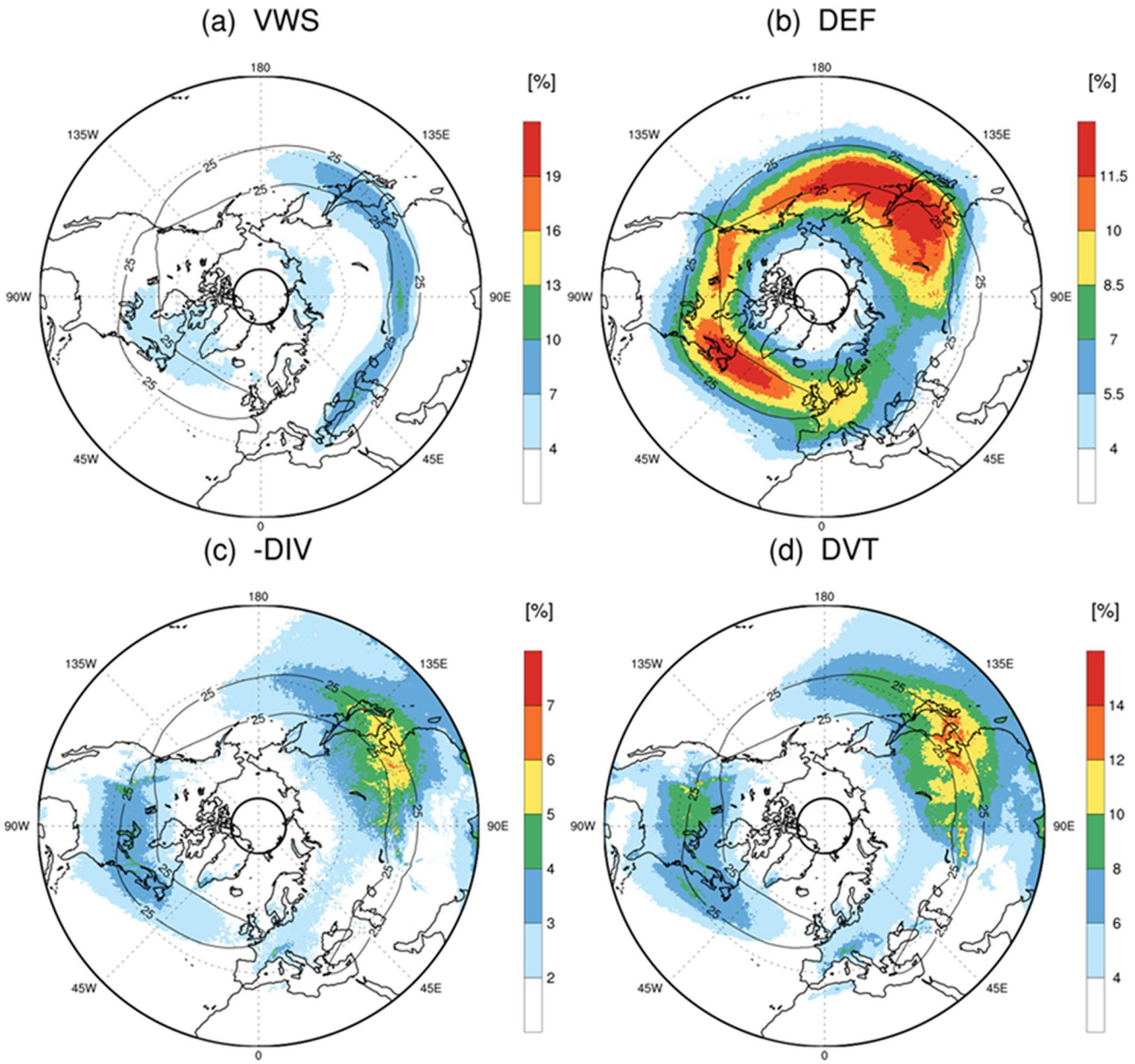

Figure 7. Same as Figure 5, but for the summer period (JJA). Distributions of averaged zonal wind speed are shown as black contour from 25 to 65 m s^{-1} at 10 m s^{-1} intervals.

East Asian jet (maximum frequency in Europe = 20.0%; East Asia = 45.4%; Eastern Pacific = 28.9%; Northwestern Atlantic = 17.1% from 100 hPa to 500 hPa in the 20–60°N; not shown). The high frequency of these large shears at all levels indicates high turbulence potential not only at the typical aircraft cruising levels of 250 hPa but also at other levels of aircraft travels over East Asia. In summer, the TI1, TI2, and TI3 distributions decreased and are shifted upward and northward along the weakened jet stream (Figure 10b). However, unlike in the winter season, DEF becomes more dominant than VWS from midlatitudes to polar regions at cruising levels as the jet core shifted upward (Figure 11b). Moreover, -DIV and DVT are broadly distributed at cruising levels at low latitudes of East Asia because of the East Asia monsoon. Due to the increased frequency of DVT, isolated patterns of TI3 at upper-levels and low latitudes of East Asia (10–30°N, 160-120 hPa) were also found. Consequently, DEF, -DIV, and DVT largely contributed to the occurrence of CAT instead of the weakened VWS in the summer.

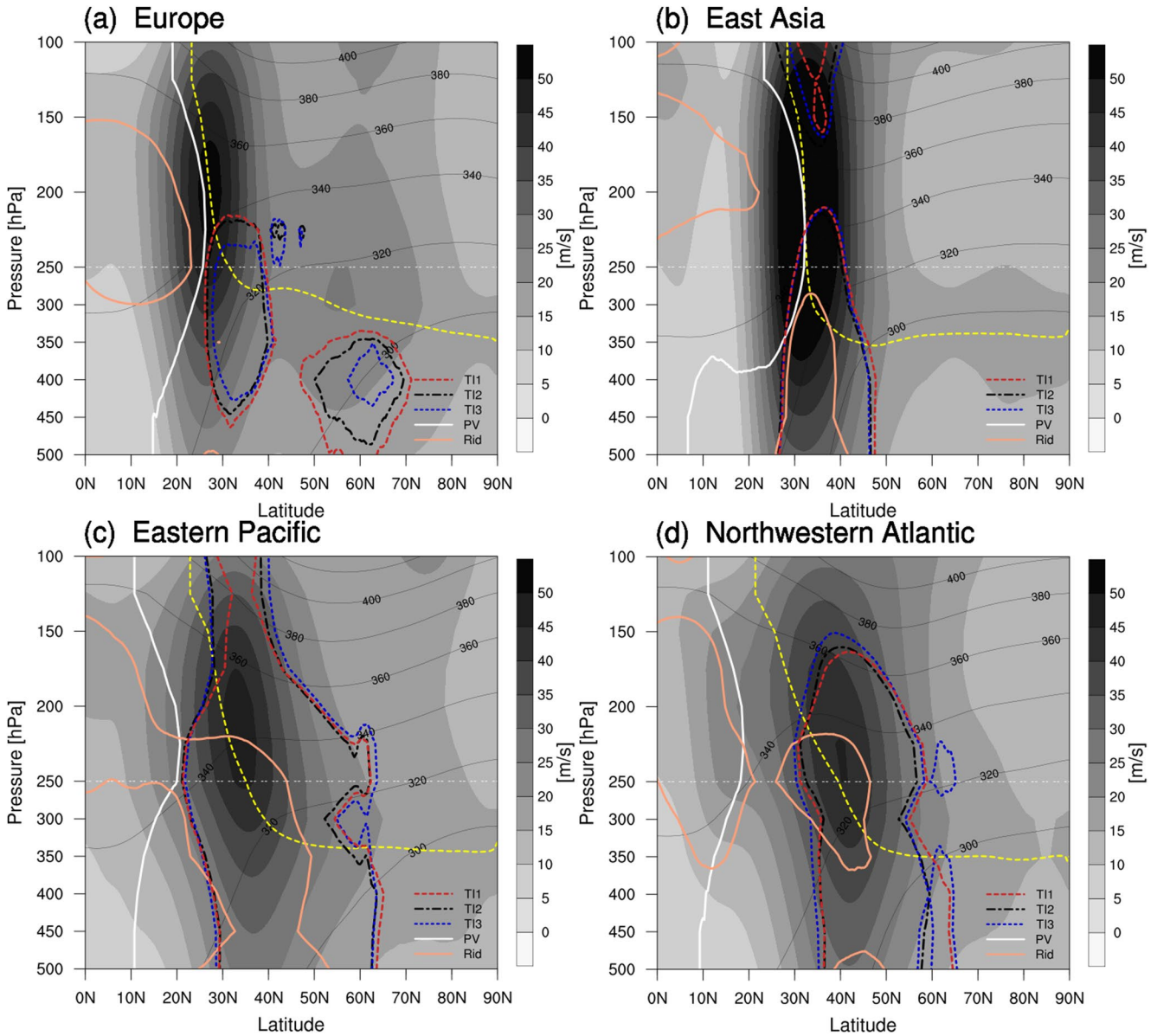

Figure 8. Vertical frequency distributions of zonally averaged Clear-Air Turbulence (CAT) indices during the winter period (DJF) for 41 years (1979–2019) [TI1 = 5% (red dashed contour), TI2 = 5% (black dashed-dotted contour), TI3 = 5% (blue dotted contour), PV = 10% (white solid contour), and Ri = 5% (pink solid contour)] and zonal wind speed (shading from 0 to 50 m s^{-1} at 5 m s^{-1} interval) for four regions: Europe [10–50°E; (a)], East Asia [120–160°E; (b)], Eastern Pacific [180°E–140°W; (c)] and Northwestern Atlantic [80–40°W; (d)]. Isentropes and two PVU tropopause are indicated by the thin gray line and yellow dashed line respectively. White thin double dotted line represents the 250 hPa level.

Over the Eastern Pacific and Northwestern Atlantic regions where jets were widely spread in the meridional direction, TI1, TI2, and TI3 were also distributed broadly from the south to north side of the jets (Figures 8c and 8d). These are roughly equally due to DEF, VWS, -DIV, and DVT at 250 hPa (Figures 9c and 9d). However, on the northern side of jet at lower levels below 250 hPa, DEF is expected to have the greatest impact on the occurrence of CAT. In summer, the areas of high frequencies of TI1, TI2, and TI3 were generally smaller and shifted to the north along the weakened jet (Figures 10c and 10d). It appears DEF was responsible for the CAT at cruising levels in summer over these regions since VWS was weakened and DEF was frequent on the northern side of the jet as was in East Asia (Figures 11c and 11d). The high frequency areas of -DIV and DVT also decreased in summer due to fewer storm tracks, which is consistent with their horizontal distributions over the Eastern Pacific and Northwestern Atlantic regions (Figures 7c and 7d).

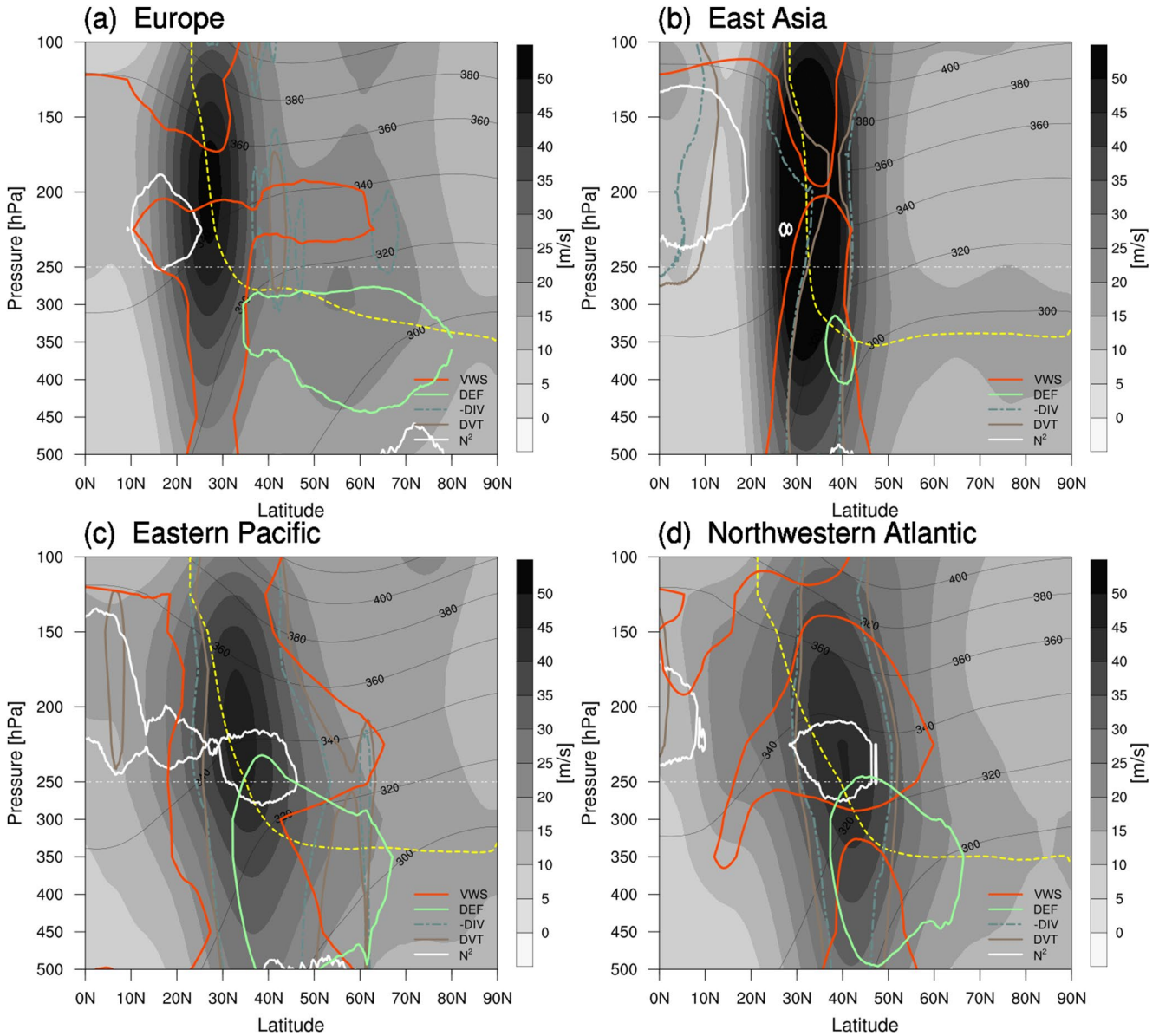

Figure 9. Same as Figure 8, but for [vertical wind shear (VWS) = 6% (orange solid contour), deformation (DEF) = 7.5% (green solid contour), -divergence (-DIV) = 3% (blue-green dashed-dotted contour), divergence tendency (DVT) = 5.5% (brown solid contour), and N^2 = 0.02% (white solid contour)] and zonal wind speed (shading from 0 to 50 m s^{-1} at 5 m s^{-1} interval).

Over Europe in winter, two maxima of empirical indices were found because of the separate subtropical (20–30°N) and polar (50–60°N) jets, leading to two maxima in the patterns of TI1, TI2, and TI3 under each jet core (Figure 8a). The patterns of TI1, TI2, and TI3 found at lower levels of the polar jet region (Figure 8a) are related to DEF on the cyclonic shear side of the subtropical jet rather than VWS (Figure 9a). On the other hand, the other maxima of TI1, TI2, and TI3 in the subtropical region (Figure 8a) are primarily associated with VWS where the stronger jet stream developed (Figure 9a). The two maximum frequencies of TI1, TI2, and TI3 were decreased in summer (Figure 10a) due to the weakened and northward shifted subtropical jet that moved northward to 30–40°N. Unlike in winter, maxima patterns of TI1, TI2, and TI3 found at upper levels above the polar jet (Figure 10a) were mainly attributed to VWS (Figure 11a).

In terms of the theoretical instability indices, areas of lowered Ri maxima were found over the Eastern Pacific and Northwestern Atlantic regions (Figures 8c and 8d) consistent with the higher frequencies of negative N^2 and larger VWS (Figures 9c and 9d) there. However, despite the presence of large VWS at all levels (Figure 10b),

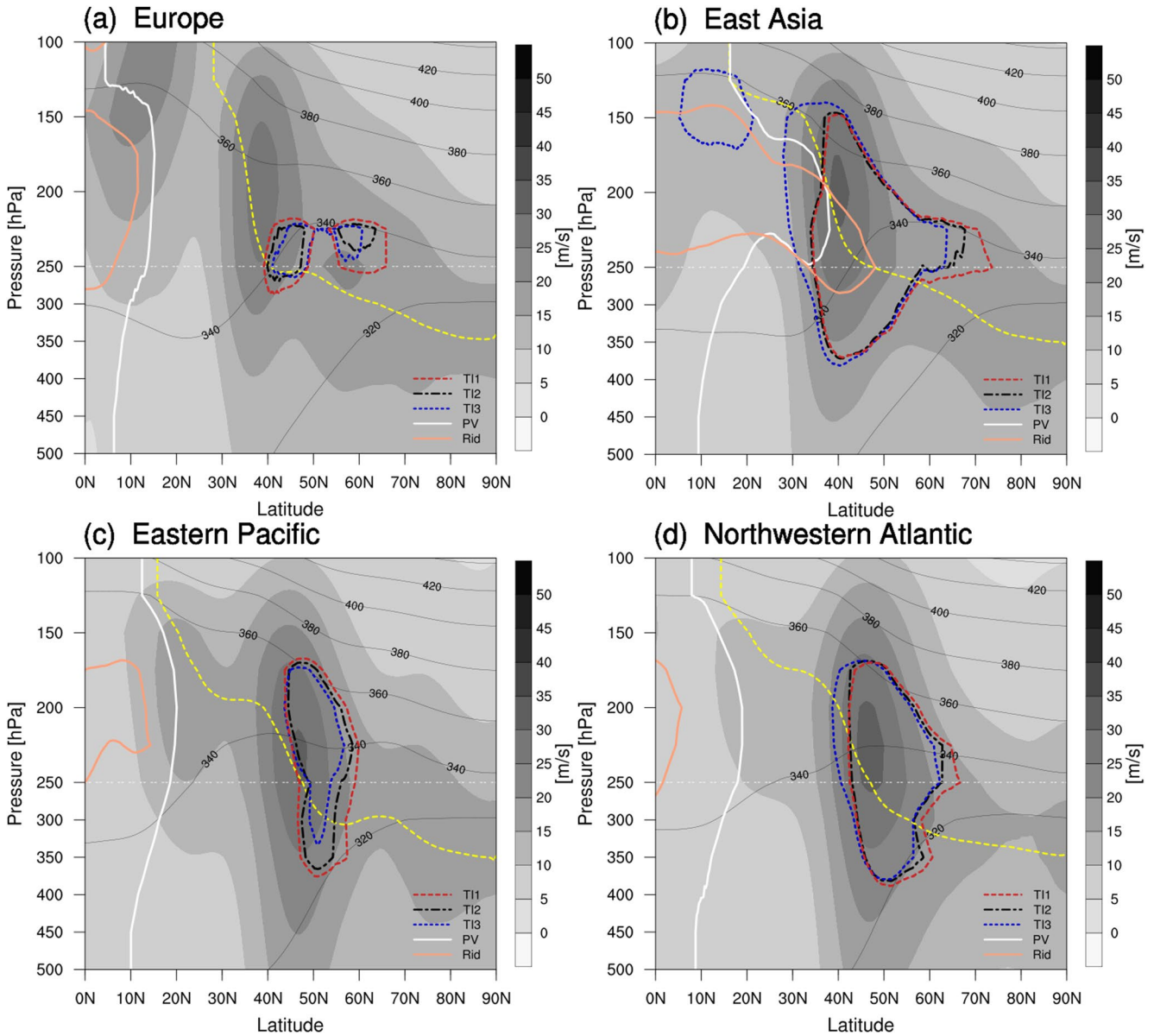

Figure 10. Same as Figure 8, but for the summer period (JJA).

smaller Ri occurs only in the troposphere below 250 hPa in the midlatitudes over East Asia (Figure 8b), while TI1, TI2, and TI3 were found at higher levels even above the tropopause indicated by the yellow dashed line. This is because tropopause folding penetrated more deeply down to 300 hPa in the 30–40°N over East Asia than in other regions (vertically erected structure of yellow dashed line), which inhibits lowered Ri due to the extremely statically stable condition over this area (i.e., tropopause folding; Kim & Chun, 2010, 2011). In contrast, as the tropopause shifted upward with a slower jet in the summer, the stability of cruising levels within the subtropical and midlatitude regions over East Asia became lower as shown in the distribution of N^2 (Figures 10b and 11b), which in turn reduced Ri so that Ri may be a more appropriate index in the summer.

The subtropical areas of East Asia are also prone to CAT by inertial/symmetric instabilities as shown in the maximum frequency of PV < 0 distributed up to 30°N in the winter period (white line in Figure 8b) because of negative absolute vorticity in the strong jet streak, while other regions were not (white lines in Figures 8a–8d). However, despite the weakened jet stream and smaller regions of negative absolute vorticity in summer, negative PV regions still occurred near 30°N on the southern side of the jet (Figure 10b). This is a consequence of low

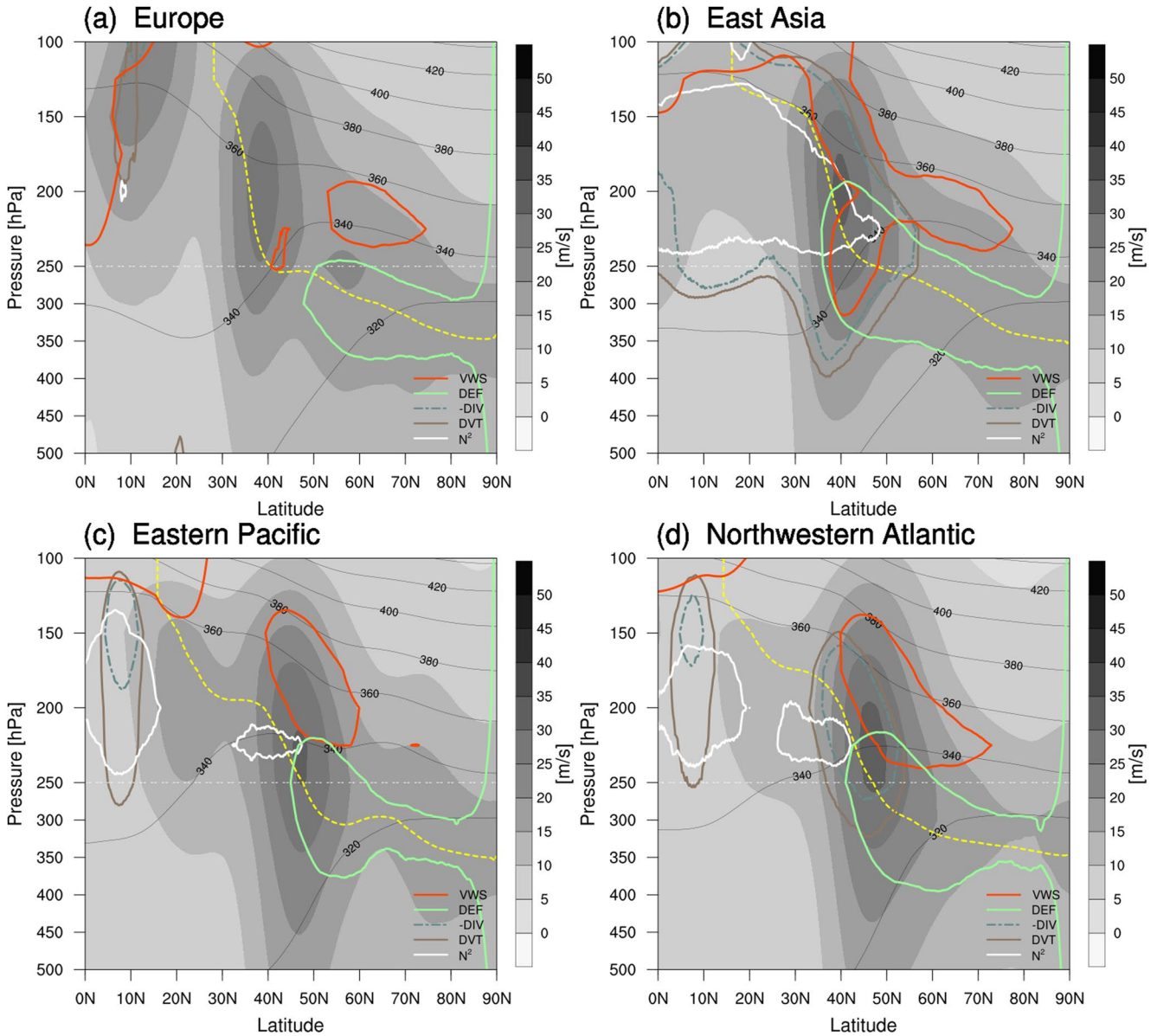

Figure 11. Same as Figure 9, but for the summer period (JJA).

stability due to the upward shift of the tropopause and instability associated with the summer monsoon. Additionally, an easterly wind over subtropical East Asia (not shown) plays a role in generating negative PV at the UTLS.

3.4. Climatological Trends

After investigating the average CAT climatology, spatial distributions, and their possible generation mechanisms relative to upper-level jet systems in the NH, we performed trend analyses to identify possible temporal changes as they may be affected by climate change over the past 41 years. Here, we analyzed winter season trends only when CAT is usually connected to jet streams. As previously mentioned, upper-level jet systems coincide with the MTG through the thermal-wind balance. Therefore, the location and intensity of jet stream may both change in a global warming scenario (e.g., Lorenz & DeWeaver, 2007; Williams & Joshi, 2013). To start then, we first computed the 41 years mean fields of MTG at 300–400 hPa (Figure 12a) and horizontal wind speed (SPD) at 250 hPa (Figure 12b). They present similar patterns implying that the upper-level jet structure is highly correlated with MTG and consequently larger VWS according to the thermal wind relation. Therefore, the DJF mean trends

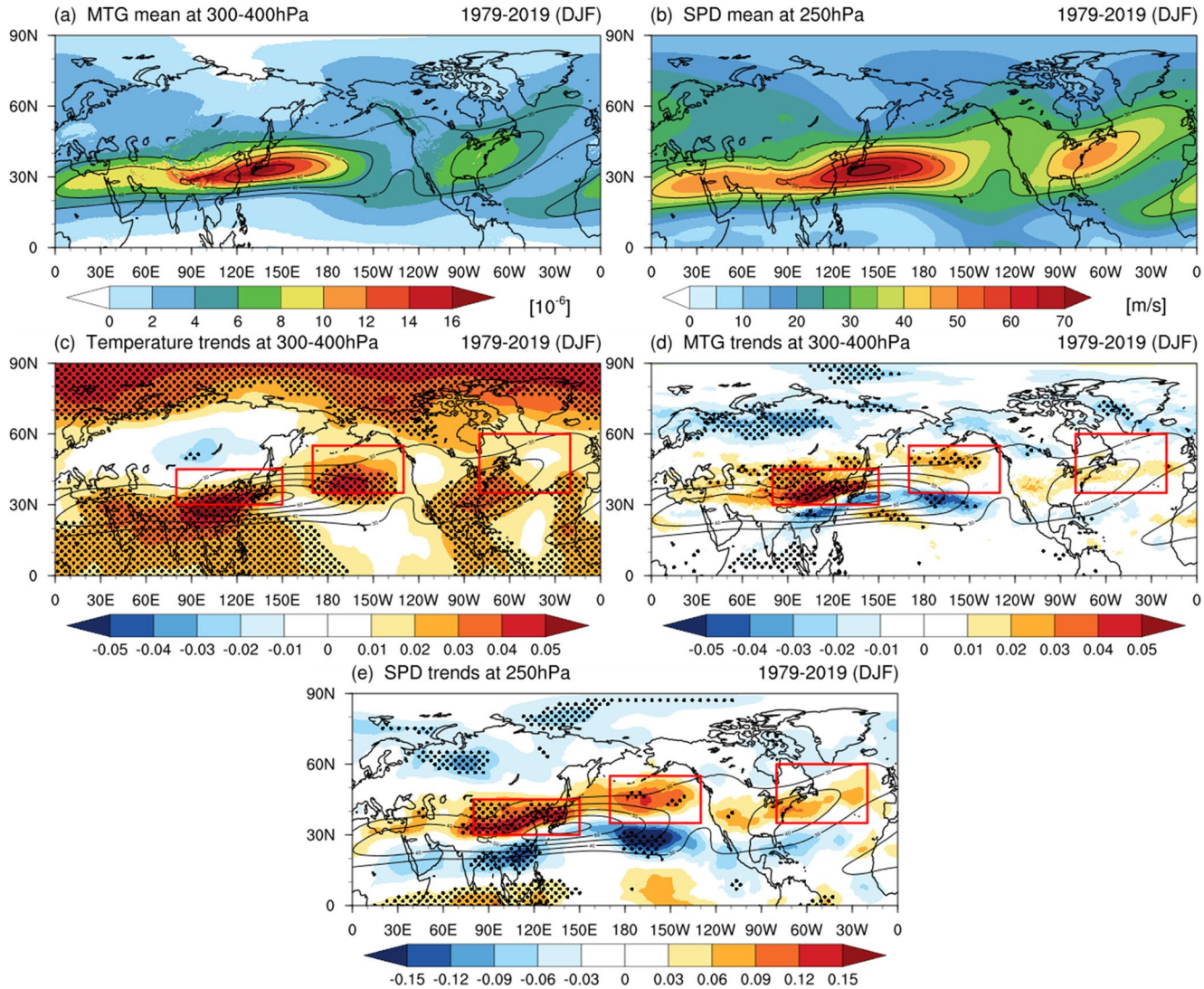

Figure 12. (a and b) Averaged meridional temperature gradient (MTG) and horizontal wind speed (SPD) at 300–400 hPa and 250 hPa for 41 years (1979–2019) respectively with shading. DJF mean trends (shading) of (c) temperature at 300–400 hPa, (d) MTG at 300–400 hPa, and (e) horizontal wind speed at 250 hPa. Black contour and stippling depict the zonal wind speed at 250 hPa (from 30 to 80 m s^{-1} with 10 m s^{-1} interval) and significant trends (P-value <0.05, $n = 41$). Red boxes in (c)–(e) indicate East Asia (80–150°E, 30–45°N), Eastern Pacific (170°E−130°W, 35–55°N), and Northwestern Atlantic (80–20°W, 35–60°N) regions from the left.

(K m^{-1} yr^{-1}) of MTG at 300–400 hPa (Figure 12d) that modulates the jet stream at 250 hPa for the 41 years was examined. Here, we computed every 41 years DJF mean of MTG and then calculated the trend using a linear least-squares regression method (Lee et al., 2019). Statistically significant trend patterns were estimated at the 95% confidence levels (P-value <0.05; $n = 41$) with a two-sided t-test (Lee et al., 2019) and these are indicated by black stippling as shown in Figure 12d. Other variables of DJF mean trends and DJF mean frequency trends were computed in the same way.

The largest increase of MTG was found over East Asia (maximum value of 0.08 K m^{-1} yr^{-1}; 80–150°E, 30–45°N), which is slightly on the northern side of the East Asian jet entrance region (Figure 12d). This is due to cooling in the middle Eurasian continent and warming in southeastern Asia regions (Figure 12c) (e.g., He et al., 2020; Kug et al., 2015; Luo et al., 2017; J. Zhang et al., 2016). Positive increases were also seen over the Eastern Pacific (maximum value of 0.03 K m^{-1} yr^{-1}; 170°E−130°W, 35–55°N) and Northwestern Atlantic (maximum value of 0.02 K m^{-1} yr^{-1}; 80–20°W, 35–60°N) regions (Figure 12d) where strong warming in the tropics and lower latitude regions have occurred (Figure 12c). Thus, as shown in Figure 12e, the jet stream has strengthened and the wind speed has increased up to 0.16 m s^{-1} per year over East Asia and 0.13 m s^{-1}, 0.10 m s^{-1} per year over the Eastern

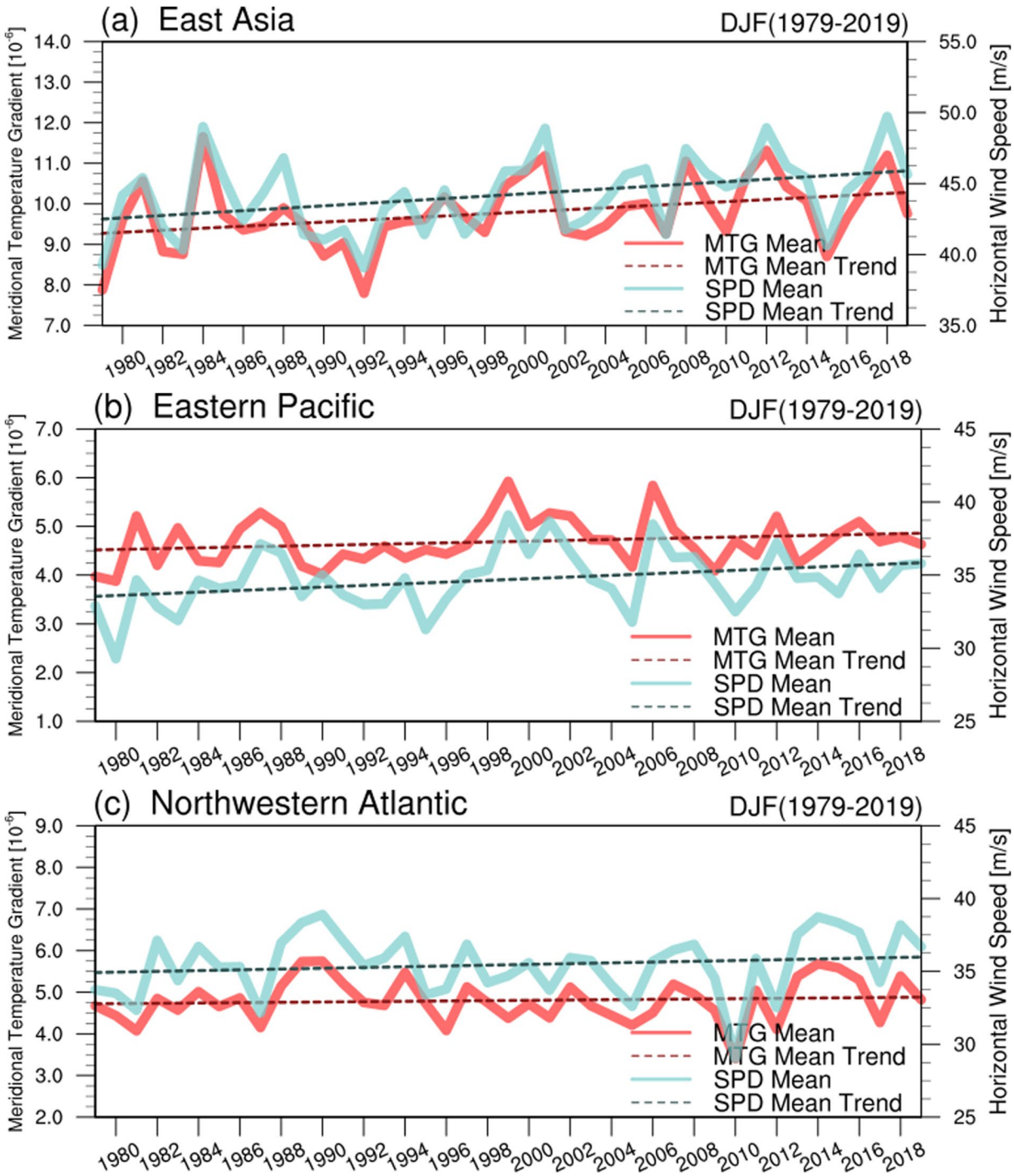

Figure 13. Time series of DJF mean meridional temperature gradient (MTG) (pink solid line), linear trends of MTG (pink dashed line), DJF mean horizontal wind speed (SPD) (light blue solid line), and linear trends of SPD (light blue dashed line) over three regions (indicated by the red boxes in Figure 12): (a) East Asia (80–150°E, 30–45°N), (b) Eastern Pacific (170°E−130°W, 35–55°N), and (c) Northwestern Atlantic (80–20°W, 35–60°N) from 1979 to 2019.

Pacific and Northwestern Atlantic due to global warming (e.g., Maloney et al., 2014; Sheffield et al., 2013). From Figure 12e, it is also apparent that the midlatitude jets have shifted northward as well as intensified.

Time series of DJF means of MTG and SPD and their trends are displayed in Figure 13 over the three regions indicated by the red boxes in Figure 12 where large variations of trends were detected. The time series of MTG and SPD were calculated by annually (for DJF) averaging each variable over a designated area and then performing

a simple linear regression to assess the trends. Over East Asia (Figure 13a) where the strongest jets exist, MTG has increased by 10.87% (S = 0.025 K m^{-1} yr^{-1}; S is slope of the regression line) and SPD has increased by 8.01% (S = 0.083 m s^{-1} yr^{-1}) over the 41 years period. Over the Eastern Pacific region (Figure 13b), MTG increased 7.59% (S = 0.008 K m^{-1} yr^{-1}) and SPD increased 6.86% (S = 0.056 m s^{-1} yr^{-1}). Over the Northwestern Atlantic region (Figure 13c), MTG increased 3.38% (S = 0.004 K m^{-1} yr^{-1}) and SPD increased 3.04% (S = 0.026 m s^{-1} yr^{-1}).

The trends in CAT indices are shown in Figure 14. Overall, the trend patterns of CAT indices affected by jet systems were demonstrated with the SPD trend at 250 hPa, as expected. Figure 15 shows box plots of increasing values of the turbulence diagnostics with time for the three regions shown in Figure 12. The box plots were calculated by regionally averaging the trends of each CAT index within designated areas shown in Figure 14. Again, East Asia showed the largest positive trend with TI1 increasing by 0.053% yr^{-1}, TI2 by 0.048% yr^{-1}, and TI3 by 0.054% yr^{-1}, all mainly due to a large increase in VWS trend 0.080% yr^{-1}, as shown in Figures 14e and 15a. The Eastern Pacific region had increases in TI1 of 0.034% yr^{-1}, TI2 of 0.029% yr^{-1}, and TI3 of 0.033% yr^{-1} which is largely driven by the trend in DEF (0.039% yr^{-1}) rather than VWS (0.007% yr^{-1}) (Figures 14e, 14f and 15b). Trends in the Northwestern Atlantic region were similar to those over the Eastern Pacific region with increases of TI1 by 0.039% yr^{-1}, TI2 by 0.034% yr^{-1}, and TI3 by 0.039% yr^{-1}, driven mainly by trends in both VWS (0.032% yr^{-1}) and DEF (0.036% yr^{-1}) as shown in Figures 14e, 14f and 15c.

In contrast, the increasing trend of Ri was highest over the Eastern Pacific region (0.048% yr^{-1}) with the lowest increase of VWS (Figure 15b). We speculate that this may be due to increased Kelvin-Helmholtz instabilities induced by lowered static stability (note that a small but positive trend in N^2 negative conditions were found for all regions in Figure 15) associated with the frequent development of cyclones along the storm tracks there. East Asia (0.022% yr^{-1}) and the Northwestern Atlantic (0.018% yr^{-1}) regions also showed Ri increases, which correspond to strengthened VWS over each area. East Asia showed a relatively low increase of Ri even though VWS has intensified significantly over the past 41 years. As previously mentioned, extremely stable condition from deep tropopause folding could disturb the identification of the shear instability trend diagnosed by Ri in UTLS over East Asia. In the case of PV, positive trends appeared along the intensified jet stream which intensifies the anticyclonic flows on the southern side of the jet. Additionally, as anticyclonic flow regions move northward, the largest reductions of PV occurred in the 20–30°N band over East Asia where maxima frequencies exist as shown in Figure 4f.

4. Summary and Conclusions

In this study, climatologies of MOG-level CAT in the UTLS were analyzed using high-resolution reanalysis ERA5 data for 41 years in the NH. To identify the occurrences of CAT and their various generation mechanisms near upper-level jets, empirical (TI1, TI2, TI3, VWS, DEF, -DIV, and DVT) and theoretical instability (Ri, PV, and N^2) diagnostics were used. The frequency distributions and trends of empirical diagnostics were investigated based on thresholds determined by calculating the top five percentile PDF value of each index at 250 hPa in the 20–60°N latitude band where long-haul flights cruise and the climatological jet streams exists. Four case studies comparing the ERA5 based turbulence diagnostics to observations of MOG-level turbulence were performed to show the selected diagnostics produced good agreement with the aircraft-based observations.

Results showed that high frequencies of the empirical indices occurred on the northern side of the jet in the winter period (DJF) and three maxima patterns were found over the East Asia, Eastern Pacific, and Northwestern Atlantic regions. The East Asia maxima coincides with the entrance region of the strongest East Asian jet and has the highest frequencies in TI1, TI2, and TI3 mainly due to large VWS. The Eastern Pacific and Northwestern Atlantic regions also have high frequencies of TI1, TI2, and TI3 largely attributed to large DEF, -DIV, and DVT at the exit of the jet stream as well as large VWS. Over these regions, the patterns of lowered Ri were consistent with the patterns of N^2 and VWS indicating low static stability induced by storm tracks and large shear instability at the exit region of the jet, respectively. On the other hand, Ri showed a minimum frequency over East Asia despite the highest frequency of VWS since the highly stable condition associated with stratospheric intrusion of stable air in the deep tropopause folds increases the value of Ri. The frequencies of negative PV (negative relative vorticity) were high on the southern side of the jet and the maximum pattern occurred over East Asia where the strongest jet streak exists. We additionally found that the high resolution of the ERA5 data can possibly detect the potential of mountain wave turbulence from the distribution of DEF, -DIV, and DVT. In summer, the overall

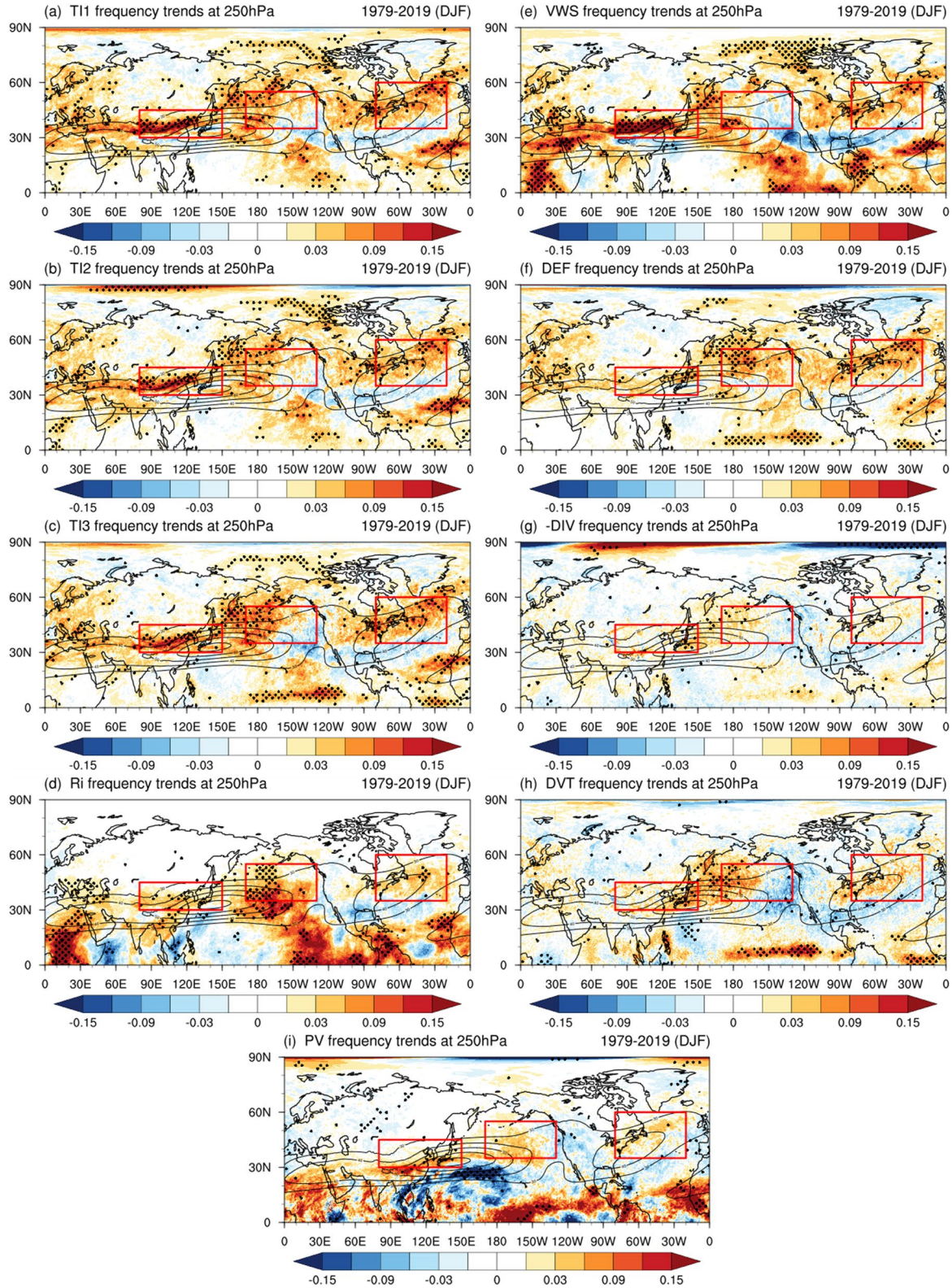

Figure 14. DJF frequency trends at 250 hPa for (a) TI1, (b) TI2, (c) TI3, (d) Richardson number (Ri), (e) vertical wind shear (VWS), (f) deformation (DEF), (g) –divergence (-DIV), (h) divergence tendency (DVT), and (i) potential vorticity (PV) (shading) over 41 years (1979–2019). Black contours and stippling depict zonal wind speed at 250 hPa (30–80 m s^{-1} at 10 m s^{-1} interval) and significant trends (P-value <0.05, $n = 41$) respectively. Red boxes indicate regions same as Figure 12.

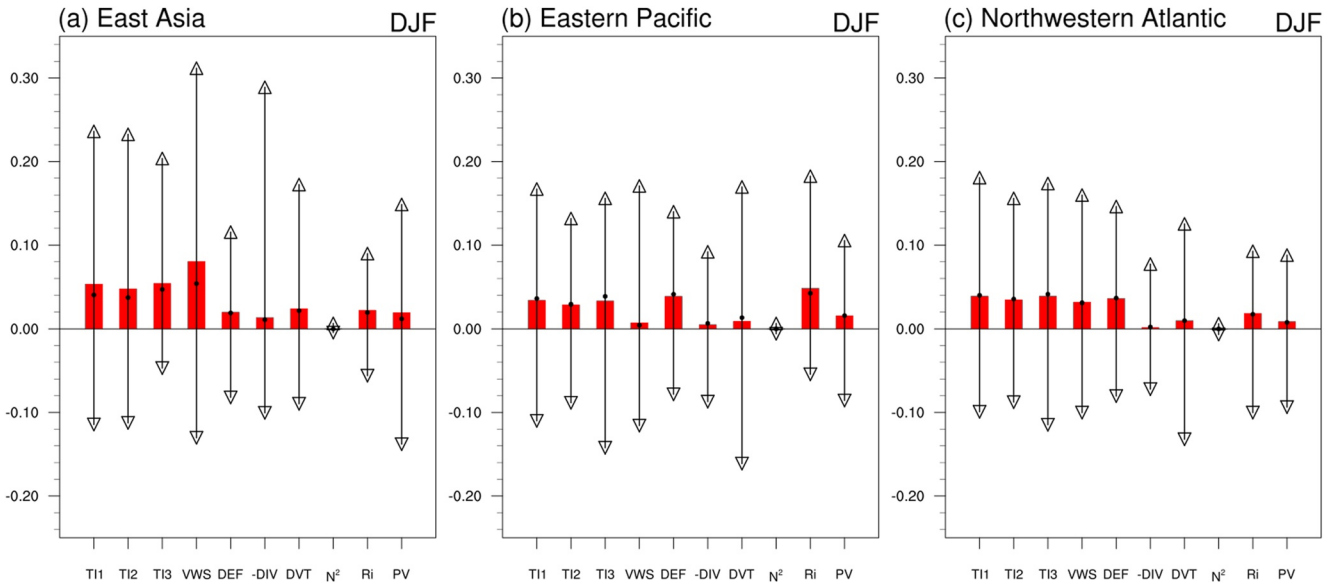

Figure 15. Box plots of 10 Clear-Air Turbulence (CAT) indices over three regions (indicated by the red boxes in Figure 14): (a) East Asia (80–150°E, 30–45°N), (b) Eastern Pacific (170°E−130°W, 35–55°N), and (c) Northwestern Atlantic (80–20°W, 35–60°N). The top and bottom of black line show the maximum and minimum frequency trend value of each index within each red box area. Red bars and black dot represent averaged frequency trend and median value of each index within each red box area respectively.

occurrence frequencies of MOG-level CAT were decreased and shifted poleward due to the northward shifted and weakened jet stream in the NH. During this season, the three maxima patterns of TI1, TI2, and TI3 were found over East Asia, Northwestern Atlantic, and Mediterranean Europe mainly due to increased DEF. Particularly East Asia had the highest CAT potential again in summer, which is primarily related to the summer monsoon system.

Next, to understand the location and intensity change of the jet stream, which leads to changes in the frequency of CAT occurrence in the UTLS, we identified a relation between SPD at 250 hPa and MTG at 300–400 hPa. As a consequence, there was an agreement between mean fields of MTG at 300–400 hPa and SPD at 250 hPa for 41 years suggesting that the upper-level jet structure is highly correlated with MTG by strengthening VWS according to thermal wind relationship. Therefore, increasing and decreasing trend patterns of SPD at 250 hPa over the past 41 years were correlated with those of the MTG trend at 300–400 hPa. The most significant increasing trend of the jet stream was found over East Asia primarily due to the enhanced VWS. This is associated with the largest increasing trend of MTG over this region and is due mainly to cooling in the middle of the eastern Eurasian continent and warming in the southeastern Asia region. Finally, although Williams (2017) and others have shown an increasing trend for CAT based on climate models over the Northwestern Atlantic region, we found that the potential of MOG-level CAT has increased the most significantly over East Asia along the intensified jet and associated increase in VWS. Relatively large increasing trends of CAT potential also appeared over the Eastern Pacific and Northwestern Atlantic regions enhanced by DEF and by both VWS and DEF respectively, which are likely due to global warming trends in these regions (e.g., Lee et al., 2019). Based on the trend patterns of CAT indices over the past 41 years, it is expected that MOG-level CAT encounters at cruising altitudes will become more common over East Asia with climate change. This trend will have a significant impact on safe transpacific flight since a dense area of air traffic across the Pacific between East Asia and the US is highly collocated with the increasing trend of VWS causing MOG-level CAT. To show this, an EDR density map was computed by counting the number of EDR values greater than zero based on AMDAR observation data covering the period from January 2016 to September 2021 (Figure 16). Therefore, for efficient and safe aviation operations it is necessary to understand the generation mechanisms of MOG-level CAT events with these trends, especially over East Asia.

We expect that this study would help to understand the response of spatial-temporal distributions and trends of CAT that occur from various generation mechanisms in the NH to climate change. Given that the number of flights has increased consistently over the past years, and is expected to continue increasing, realizing a linkage

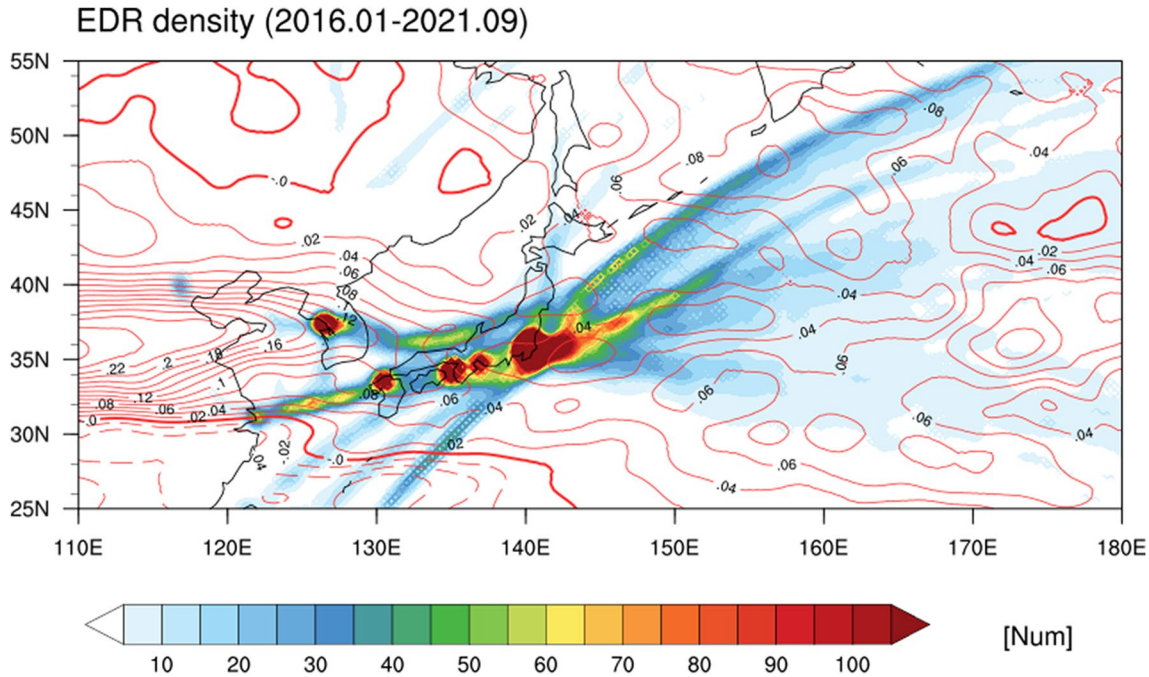

Figure 16. Eddy Dissipation Rate (EDR) (>0 $m^{2/3}s^{-1}$) distribution (shading) from Aircraft Meteorological Data Reports (AMDAR) data with winter VWS trend (contour; negative values are indicated by dash contours) (from January 2016 to September 2021).

between climate change and aviation turbulence becomes more important. We suggest that further studies of climatology in cloud-induced turbulence and mountain wave turbulence which are also major sources of aviation turbulence (Doyle et al., 2005; Kim & Chun, 2011; Kim et al., 2014) are needed. Though they were not covered in this study, they also might be highly sensitive to climate change. Finally, the climatology of CAT based on observational data will be studied in the future to determine if it is consistent with the results analyzed by reanalysis data, as done for North Atlantic winds by Tenenbaum et al. (2022) and others.

Data Availability Statement

The fifth generation ECMWF reanalysis hourly data (ERA5) on pressure levels can be downloaded at https://cds.climate.copernicus.eu/cdsapp#!/dataset/10.24381/cds.bd0915c6?tab=overview [Dataset]. Aircraft Meteorological Data Reports (AMDAR) data can be accessed from https://data.eol.ucar.edu/dataset/100.016 [Dataset].

Acknowledgments
This work was supported by the Basic Science Research Program through the National Research Foundation of Korea (NRF), funded by the Ministry of Education (NRF-2019R1I1A2A1060035) and the Korea government (MSIT) (NRF-2021R1A4A5032320). This work was also funded by the Korea Meteorological Administration Research and Development Program under Grant KMI2022-00410.

References

Abarbanel, H. D. I., Holm, D. D., Marsden, J. E., & Ratiu, T. (1984). Richardson number criterion for the nonlinear stability of three-dimensional stratified flow. *Physical Review Letters*, *52*(26), 2352–2355. https://doi.org/10.1103/PhysRevLett.52.2352

Cho, J. Y. N., & Lindborg, E. (2001). Horizontal velocity structure functions in the upper troposphere and lower stratosphere: 1. Observations. *Journal of Geophysical Research*, *106*(D10), 10223–10232. https://doi.org/10.1029/2000JD900814

Colson, D. (1963). Analysis of clear air turbulence data for March 1962. *Monthly Weather Review*, *91*(2), 73–82. https://doi.org/10.1175/1520-0493(1963)091<0073:AOCATD>2.3.CO;2

Doyle, J. D., Shapiro, M. A., Jiang, Q., & Bartels, D. L. (2005). Large-amplitude mountain wave breaking over Greenland. *Journal of the Atmospheric Sciences*, *62*(9), 3106–3126. https://doi.org/10.1175/JAS3528.1

Dutton, J. A., & Panofsky, H. A. (1970). Clear air turbulence: A mystery may be unfolding: High altitude turbulence poses serious problems for aviation and atmospheric science. *Science*, *167*(3920), 937–944. https://doi.org/10.1126/science.167.3920.937

Ellrod, G. P. (1985). *Detection of high level turbulence using satellite imagery and upper air data*. National Environmental Satellite and Information Service. Retrieved from https://repository.library.noaa.gov/view/noaa/32485

Ellrod, G. P., & Knapp, D. I. (1992). An objective clear-air turbulence forecasting technique: Verification and operational use. *Weather and Forecasting*, *7*(1), 150–165. https://doi.org/10.1175/1520-0434(1992)007<0150:AOCATF>2.0.CO;2

Ellrod, G. P., & Knox, J. A. (2010). Improvements to an operational clear-air turbulence diagnostic index by addition of a divergence trend term. *Weather and Forecasting*, *25*(2), 789–798. https://doi.org/10.1175/2009WAF2222290.1

He, S., Xu, X., Furevik, T., & Gao, Y. (2020). Eurasian cooling linked to the vertical distribution of Arctic warming. *Geophysical Research Letters*, *47*(10), e2020GL087212. https://doi.org/10.1029/2020GL087212

Hersbach, H., Bell, B., Berrisford, P., Hirahara, S., Horányi, A., Muñoz-Sabater, J., et al. (2020). The ERA5 global reanalysis. *Quarterly Journal of the Royal Meteorological Society*, *146*(730), 1999–2049. https://doi.org/10.1002/qj.3803

Holton, J. R. (1992). *An introduction to dynamic meteorology. International Geophysics Series 16*. Elsevier.

Hoskins, B. J., & Hodges, K. I. (2019). The annual cycle of Northern Hemisphere storm tracks. Part I: Seasons. *Journal of Climate*, *32*(6), 1743–1760. https://doi.org/10.1175/JCLI-D-17-0870.1

Jaeger, E. B., & Sprenger, M. (2007). A Northern Hemispheric climatology of indices for clear air turbulence in the tropopause region derived from ERA40 reanalysis data. *Journal of Geophysical Research*, *112*(D20), D20106. https://doi.org/10.1029/2006JD008189

Kim, J.-H., Chan, W. N., Sridhar, B., Sharman, R. D., Williams, P. D., & Strahan, M. (2016). Impact of the North Atlantic Oscillation on transatlantic flight routes and clear-air turbulence. *Journal of Applied Meteorology and Climatology*, *55*(3), 763–771. https://doi.org/10.1175/JAMC-D-15-0261.1

Kim, J.-H., & Chun, H.-Y. (2010). A numerical study of clear-air turbulence (CAT) encounters over South Korea on 2 April 2007. *Journal of Applied Meteorology and Climatology*, *49*(12), 2381–2403. https://doi.org/10.1175/2010JAMC2449.1

Kim, J.-H., & Chun, H.-Y. (2011). Statistics and possible sources of aviation turbulence over South Korea. *Journal of Applied Meteorology and Climatology*, *50*(2), 311–324. https://doi.org/10.1175/2010JAMC2492.1

Kim, J.-H., & Chun, H.-Y. (2012). A numerical simulation of convectively induced turbulence above deep convection. *Journal of Applied Meteorology and Climatology*, *51*(6), 1180–1200. https://doi.org/10.1175/JAMC-D-11-0140.1

Kim, J.-H., Chun, H.-Y., Sharman, R. D., & Keller, T. L. (2011). Evaluations of upper-level turbulence diagnostics performance using the Graphical Turbulence Guidance (GTG) system and pilot reports (PIREPs) over East Asia. *Journal of Applied Meteorology and Climatology*, *50*(9), 1936–1951. https://doi.org/10.1175/JAMC-D-10-05017.1

Kim, J.-H., Chun, H.-Y., Sharman, R. D., & Trier, S. B. (2014). The role of vertical shear on aviation turbulence within cirrus bands of a simulated western Pacific cyclone. *Monthly Weather Review*, *142*(8), 2794–2813. https://doi.org/10.1175/mwr-d-14-00008.1

Kim, J.-H., Kim, D., Lee, D.-B., Chun, H.-Y., Sharman, R. D., Williams, P. D., & Kim, Y.-J. (2020). Impact of climate variabilities on trans-oceanic flight times and emissions during strong NAO and ENSO phases. *Environmental Research Letters*, *15*(10), 105017. https://doi.org/10.1088/1748-9326/abaa77

Kim, J.-H., Sharman, R., Strahan, M., Scheck, J. W., Bartholomew, C., Cheung, J. C. H., et al. (2018). Improvements in nonconvective aviation turbulence prediction for the world area forecast system. *Bulletin of the American Meteorological Society*, *99*(11), 2295–2311. https://doi.org/10.1175/BAMS-D-17-0117.1

Kim, S.-H., Kim, J., Kim, J.-H., & Chun, H.-Y. (2022). Characteristics of the derived energy dissipation rate using the 1 Hz commercial aircraft quick access recorder (QAR) data. *Atmospheric Measurement Techniques*, *15*(7), 2277–2298. https://doi.org/10.5194/amt-15-2277-2022

Knox, J. A. (1997). Possible mechanisms of clear-air turbulence in strongly anticyclonic flows. *Monthly Weather Review*, *125*(6), 1251–1259. https://doi.org/10.1175/1520-0493(1997)125<1251:PMOCAT>2.0.CO;2

Knox, J. A., & Harvey, V. L. (2005). Global climatology of inertial instability and Rossby wave breaking in the stratosphere. *Journal of Geophysical Research*, *110*(D6). https://doi.org/10.1029/2004JD005068

Knox, J. A., McCann, D. W., & Williams, P. D. (2008). Application of the Lighthill–Ford theory of spontaneous imbalance to clear-air turbulence forecasting. *Journal of the Atmospheric Sciences*, *65*(10), 3292–3304. https://doi.org/10.1175/2008JAS2477.1

Koch, S. E., Jamison, B. D., Lu, C., Smith, T. L., Tollerud, E. I., Girz, C., et al. (2005). Turbulence and gravity waves within an upper-level front. *Journal of the Atmospheric Sciences*, *62*(11), 3885–3908. https://doi.org/10.1175/JAS3574.1

Kug, J.-S., Jeong, J.-H., Jang, Y.-S., Kim, B.-M., Folland, C. K., Min, S.-K., & Son, S.-W. (2015). Two distinct influences of Arctic warming on cold winters over North America and East Asia. *Nature Geoscience*, *8*(10), 759–762. https://doi.org/10.1038/ngeo2517

Lane, T. P., Doyle, J. D., Plougonven, R., Shapiro, M. A., & Sharman, R. D. (2004). Observations and numerical simulations of inertia–gravity waves and shearing instabilities in the vicinity of a jet stream. *Journal of the Atmospheric Sciences*, *61*(22), 2692–2706. https://doi.org/10.1175/JAS3305.1

Lane, T. P., Sharman, R. D., Trier, S. B., Fovell, R. G., & Williams, J. K. (2012). Recent advances in the understanding of near-cloud turbulence. *Bulletin of the American Meteorological Society*, *93*(4), 499–515. https://doi.org/10.1175/BAMS-D-11-00062.1

Lee, D.-B., & Chun, H.-Y. (2015). A statistical analysis of aviation turbulence observed in pilot report (PIREP) over East Asia including South Korea. *Atmosphere*, *25*(1), 129–140. https://doi.org/10.14191/ATMOS.2015.25.1.129

Lee, D.-B., Chun, H.-Y., & Kim, J.-H. (2020). Evaluation of multimodel-based ensemble forecasts for clear-air turbulence. *Weather and Forecasting*, *35*(2), 507–521. https://doi.org/10.1175/WAF-D-19-0155.1

Lee, S. H., Williams, P. D., & Frame, T. H. A. (2019). Increased shear in the North Atlantic upper-level jet stream over the past four decades. *Nature*, *572*(7771), 639–642. https://doi.org/10.1038/s41586-019-1465-z

Lester, P. F. (1994). *Turbulence: A new perspective for pilots*. Jeppesen Sanderson.

Lorenz, D. J., & DeWeaver, E. T. (2007). Tropopause height and zonal wind response to global warming in the IPCC scenario integrations. *Journal of Geophysical Research*, *112*(D10). https://doi.org/10.1029/2006JD008087

Luo, D., Chen, Y., Dai, A., Mu, M., Zhang, R., & Ian, S. (2017). Winter Eurasian cooling linked with the Atlantic Multidecadal Oscillation. *Environmental Research Letters*, *12*(12), 125002. https://doi.org/10.1088/1748-9326/aa8de8

Lv, Y., Guo, J., Li, J., Han, Y., Xu, H., Guo, X., et al. (2021). Increased turbulence in the Eurasian upper-level jet stream in winter: Past and future. *Earth and Space Science*, *8*(2), e2020EA001556. https://doi.org/10.1029/2020EA001556

Maloney, E. D., Camargo, S. J., Chang, E., Colle, B., Fu, R., Geil, K. L., et al. (2014). North American climate in CMIP5 experiments: Part III: Assessment of twenty-first-century projections. *Journal of Climate*, *27*(6), 2230–2270. https://doi.org/10.1175/JCLI-D-13-00273.1

NOAA/Earth System Research Laboratory. (2011). Aircraft Meteorological Data Reports (AMDAR) and Aircraft Communications Addressing and Reporting System (ACARS) Data. Version 1.0 (1.0) [Dataset]. UCAR/NCAR - Earth Observing Laboratory. https://doi.org/10.26023/5FSS-TF0N-V906

Prein, A. F., Liu, C., Ikeda, K., Bullock, R., Rasmussen, R. M., Holland, G. J., & Clark, M. (2020). Simulating North American mesoscale convective systems with a convection-permitting climate model. *Climate Dynamics*, *55*(1), 95–110. https://doi.org/10.1007/s00382-017-3993-2

Sato, K., & Dunkerton, T. J. (2002). Layered structure associated with low potential vorticity near the tropopause seen in high-resolution radiosondes over Japan. *Journal of the Atmospheric Sciences*, *59*(19), 2782–2800. https://doi.org/10.1175/1520-0469(2002)059<2782:LSAWLP>2.0.CO;2

Sharman, R. D., Cornman, L. B., Meymaris, G., Pearson, J., & Farrar, T. (2014). Description and derived climatologies of automated in situ eddy-dissipation-rate reports of atmospheric turbulence. *Journal of Applied Meteorology and Climatology*, *53*(6), 1416–1432. https://doi.org/10.1175/JAMC-D-13-0329.1

Sharman, R. D., & Pearson, J. M. (2017). Prediction of energy dissipation rates for aviation turbulence. Part I: Forecasting nonconvective turbulence. *Journal of Applied Meteorology and Climatology*, *56*(2), 317–337. https://doi.org/10.1175/JAMC-D-16-0205.1

Sharman, R., Tebaldi, C., Wiener, G., & Wolff, J. (2006). An integrated approach to mid- and upper-level turbulence forecasting. *Weather and Forecasting*, *21*(3), 268–287. https://doi.org/10.1175/WAF924.1

Sharman, R. D., Trier, S. B., Lane, T. P., & Doyle, J. D. (2012). Sources and dynamics of turbulence in the upper troposphere and lower stratosphere: A review. *Geophysical Research Letters*, *39*(12). https://doi.org/10.1029/2012GL051996

Sheffield, J., Barrett, A. P., Colle, B., Nelun Fernando, D., Fu, R., Geil, K. L., et al. (2013). North American climate in CMIP5 experiments. Part I: Evaluation of historical simulations of continental and regional climatology. *Journal of Climate*, *26*(23), 9209–9245. https://doi.org/10.1175/JCLI-D-12-00592.1

Storer, L. N., Williams, P. D., & Joshi, M. M. (2017). Global response of clear-air turbulence to climate change. *Geophysical Research Letters*, *44*(19), 9976–9984. https://doi.org/10.1002/2017GL074618

Tenenbaum, J., Williams, P. D., Turp, D., Buchanan, P., Coulson, R., Gill, P. G., et al. (2022). Aircraft observations and reanalysis depictions of trends in the North Atlantic winter jet stream wind speeds and turbulence. *Quarterly Journal of the Royal Meteorological Society*, *148*(747), 2927–2941. https://doi.org/10.1002/qj.4342

Thompson, C. F., Schultz, D. M., & Vaughan, G. (2018). A global climatology of tropospheric inertial instability. *Journal of the Atmospheric Sciences*, *75*(3), 805–825. https://doi.org/10.1175/JAS-D-17-0062.1

Tian, B., Held, I. M., Lau, N.-C., & Soden, B. J. (2005). Diurnal cycle of summertime deep convection over North America: A satellite perspective. *Journal of Geophysical Research*, *110*(D8), D08108. https://doi.org/10.1029/2004JD005275

Trier, S. B., & Sharman, R. D. (2016). Mechanisms influencing cirrus banding and aviation turbulence near a convectively enhanced upper-level jet stream. *Monthly Weather Review*, *144*(8), 3003–3027. https://doi.org/10.1175/MWR-D-16-0094.1

Trier, S. B., Sharman, R. D., Muñoz-Esparza, D., & Keller, T. L. (2022). Effects of distant organized convection on forecasts of widespread clear-air turbulence. *Monthly Weather Review*, *150*(10), 2593–2615. https://doi.org/10.1175/MWR-D-22-0077.1

Williams, P. D. (2017). Increased light, moderate, and severe clear-air turbulence in response to climate change. *Advances in Atmospheric Sciences*, *34*(5), 576–586. https://doi.org/10.1007/s00376-017-6268-2

Williams, P. D., & Joshi, M. M. (2013). Intensification of winter transatlantic aviation turbulence in response to climate change. *Nature Climate Change*, *3*(7), 644–648. https://doi.org/10.1038/nclimate1866

Wolff, J. K., & Sharman, R. D. (2008). Climatology of upper-level turbulence over the contiguous United States. *Journal of Applied Meteorology and Climatology*, *47*(8), 2198–2214. https://doi.org/10.1175/2008JAMC1799.1

Yihui, D., & Chan, J. C. L. (2005). The East Asian summer monsoon: An overview. *Meteorology and Atmospheric Physics*, *89*(1), 117–142. https://doi.org/10.1007/s00703-005-0125-z

Zhang, F. (2004). Generation of mesoscale gravity waves in upper-tropospheric jet–front systems. *Journal of the Atmospheric Sciences*, *61*(4), 440–457. https://doi.org/10.1175/1520-0469(2004)061<0440:GOMGWI>2.0.CO;2

Zhang, J., Tian, W., Chipperfield, M. P., Xie, F., & Huang, J. (2016). Persistent shift of the Arctic polar vortex towards the Eurasian continent in recent decades. *Nature Climate Change*, *6*(12), 1094–1099. https://doi.org/10.1038/nclimate3136